



HAL
open science

Formation of microbial organic carbonates during the Late Jurassic from the Northern Tethys (Amu Darya Basin, Uzbekistan): implications for Jurassic anoxic events.

Mehdi Carmeille, Raphaël Bourillot, Pierre Pellenard, Victor Dupias, Johann Schnyder, Laurent Riquier, Olivier Mathieu, Marie-Françoise Brunet, Raymond Enay, Vincent Grossi, et al.

► **To cite this version:**

Mehdi Carmeille, Raphaël Bourillot, Pierre Pellenard, Victor Dupias, Johann Schnyder, et al.. Formation of microbial organic carbonates during the Late Jurassic from the Northern Tethys (Amu Darya Basin, Uzbekistan): implications for Jurassic anoxic events.. *Global and Planetary Change*, 2020, 186, pp.103127. 10.1016/j.gloplacha.2020.103127. hal-02511298

HAL Id: hal-02511298

<https://hal.science/hal-02511298v1>

Submitted on 6 Nov 2020

HAL is a multi-disciplinary open access archive for the deposit and dissemination of scientific research documents, whether they are published or not. The documents may come from teaching and research institutions in France or abroad, or from public or private research centers.

L'archive ouverte pluridisciplinaire **HAL**, est destinée au dépôt et à la diffusion de documents scientifiques de niveau recherche, publiés ou non, émanant des établissements d'enseignement et de recherche français ou étrangers, des laboratoires publics ou privés.

1 Formation of microbial organic carbonates during the
2 Late Jurassic from the Northern Tethys (Amu Darya
3 Basin, Uzbekistan): Implications for Jurassic anoxic
4 events

5

6 Mehdi Carmelle^(a), Raphaël Bourillot^(a), Pierre Pellenard^(b), Victor Dupias^(b), Johann
7 Schnyder^(c), Laurent Riquier^(c), Olivier Mathieu^(b), Marie-Françoise Brunet^(c), Raymond
8 Enay^(d), Vincent Grossi^(d), Cécile Gaborieau^(e), Philippe Razin^(a), Pieter T. Visscher^(b, f)

9 ^a EA 4592 Géoressources & Environnement, ENSEGID, Bordeaux INP, 1, allée F. Daguin, 33607 Pessac Cedex, France

10 ^b UMR CNRS 6282 Biogéosciences, Université de Bourgogne Franche-Comté, 6, Bd Gabriel, 21000 Dijon, France

11 ^c Sorbonne Université, CNRS-INSU, Institut des Sciences de la Terre de Paris, iSTeP, 4 place Jussieu, 75005 Paris, France

12 ^d LGL-TPE-Laboratoire de Géologie de Lyon – Terre, Planètes, Environnement, UMR CNRS 5276, Université Claude Bernard,
13 Lyon 1, 2, rue Raphaël Dubois, 69622 Villeurbanne Cedex, France

14 ^e I2M, UMR CNRS 5295, Esplanade des Arts et Métiers, 33405 Talence Cedex, France

15 ^f Department of Marine Sciences, University of Connecticut, 1080 Shennecossett Road, Groton, CT 06340, USA.

16

17 **ABSTRACT**

18 The Late Jurassic was a period of major global carbon cycle perturbations with episodes of anoxia
19 leading to regional accumulation of organic matter in sediments worldwide. The Tubiegatan section
20 (SW Gissar Mountains, Uzbekistan) located in the Northern Tethys, shows atypical organic-rich
21 limestone and marl deposits (up to 6% of total organic carbon) marked by pronounced **negative**
22 excursions of $\delta^{13}\text{C}_{\text{carb}}$ (amplitude of *ca.* 12‰) and $\delta^{13}\text{C}_{\text{org}}$ (amplitude of *ca.* 4‰) recorded during the
23 Middle Oxfordian (Transversarium Zone). A transdisciplinary approach including sedimentology,
24 palynofacies characterization, mineralogy, organic and inorganic geochemistry was carried out to
25 elucidate the origin of these organic-rich deposits. Highest TOC are measured in nodular limestones,
26 and lowest $\delta^{13}\text{C}_{\text{carb}}$ values in thinly laminated facies consisting in alternances of infra-millimeter-thick
27 organic and carbonate laminae. In the latter, the presence of organic-carbonate peloids and of possible
28 remnants of exopolymeric substances associated with clay indicate that these structures are probably
29 mineralized **laminated** benthic microbial mats (i.e., stromatolites). Rock-Eval pyrolysis coupled to
30 palynofacies analyses point to a dominant altered marine organic matter of probable algal/microbial

31 origin, with subordinate continental phytoclasts inputs in the upper part of the organic-rich interval.
32 Trace elements (U/Th, V/Cr and Mo/Al ratios) indicate two anoxic episodes coinciding with the highest
33 TOC, punctuated by dysoxic periods. Such O₂-depleted conditions have allowed the preservation and
34 probably the development of anaerobic microbial communities in the microbial mats. In these latter,
35 **sulfate reduction probably had a significant contribution to the production of carbonates**, which would
36 explain the **precipitation** of pyrite and the **relatively** low $\delta^{13}\text{C}_{\text{carb}}$ values. The progressive decrease then
37 disappearance of kaolinite from the base of the organic-rich interval, is interpreted as a progressive
38 aridification of the Amu Darya Basin during the Transversarium Zone, culminating with the
39 progradation of a large-scale gypsum sabkha overlying the organic deposits. Overall, the organic-rich
40 deposits could record the onset of the disconnection of the Amu Darya Basin from the open sea to the
41 south, induced by compression and subsequent uplifts in the Afghan and Central Iranian blocks. The
42 elevated evaporation, coupled with the presence of hydrological barriers (such as coral reefs) could have
43 led to the formation of local **to regional anoxic conditions in the Amu Darya Basin**. Similar microbial
44 organic accumulations are **recently known** throughout the Tethys (e.g., Arabian Plate, Western Europe)
45 and from other oceans (e.g., Central Atlantic, Pacific) during the Late Jurassic, suggesting common
46 controlling factors. **The increase of** organic matter storage worldwide coupled with potential methane
47 release could have in turn induced major perturbations of the carbon cycle during the Oxfordian-
48 Kimmeridgian interval. The relatively shallow anoxia model proposed in this study contrasts with the
49 well-known organic carbon-rich pelagic models proposed for the Jurassic anoxia (e.g., Toarcian,
50 Kimmeridgian) and Cretaceous OAEs.

51

52 **Keywords:** Late Jurassic, Amu Darya Basin, microbial/laminated sediments, organic-rich carbonates,
53 anoxia, stable isotopes

54 **1. INTRODUCTION**

55 The Late Jurassic is a period marked by **multiple** anoxic events (e.g., Trabucho-Alexandre et al., 2012;
56 Martinez & Dera, 2015). More specifically, the Oxfordian and Kimmeridgian Stages are characterized
57 by episodes of regional anoxia resulting in the accumulation and preservation of organic matter (OM)

58 in several sedimentary formations throughout the world, e.g., the Staffin Shale Fm. (Middle Callovian–
59 Lower Kimmeridgian, Isle of Skye, Scotland; Pearce et al., 2005), the Knollenkalk Fm. (Middle
60 Oxfordian, Jura, Switzerland; Rais et al., 2007), La Manga Fm. (Middle–Upper Oxfordian, Neuquen
61 Basin, Argentina; Palma et al., 2015), the Hanifa Fm. (Oxfordian–Lower Kimmeridgian, Central
62 Arabian Basin, Saudi Arabia; Droste, 1990; Vahrenkamp et al., 2015), the Smackover Fm. (Oxfordian–
63 Kimmeridgian, Gulf Coast, USA; Oehler, 1984), the Spiti Shale Fm. (Oxfordian–Berriasian, Malla
64 Johar, India; Jain et al., 1984), the Akkuyu Fm. (Lower Kimmeridgian–Tithonian, Taurus Mountains,
65 Turkey; Baudin et al., 1999), the Kimmeridge Clay Fm. (Kimmeridgian–Tithonian, Dorset, UK;
66 Tribovillard et al., 1994). A large number of these organic rocks show a fine-grained laminated fabric,
67 sometimes called organic varves. This facies has been interpreted as mineralized microbial mats (or
68 stromatolites) that formed in shallow stratified, hypersaline lagoons (Bernier and Enay, 1972;
69 Tribovillard et al., 2000; Warren, 2011). Warren (2011) postulated that such laminated organic
70 sediments could also reflect pronounced seasonal **salinity and nutrient variations** leading to blooms in
71 primary productivity, which in turn would result in the formation of organic laminae.

72 At the global scale, the role of climate and tectonic on the multiplication of organic-rich formations
73 during the Late Jurassic is still debated. On the Arabian platform, the Hanifa and Jubaila Fms. have
74 accumulated in partially isolated **and stratified** intrashelf basins. In a recent review, Vahrenkamp et al.
75 (2015) link the formation of such basins to a tectonic uplift at the margin of the Arabian Plate. Based on
76 the presence of biosiliceous deposits, Eltom et al. (2017) have related the elevated organic productivity
77 in these basins to regional upwellings developing at the shelf edge. Both models may explain the
78 formation of organic sediments on large epeiric platforms (Warren, 2011). In addition, several authors
79 proposed that the increase in organic productivity and the multiple anoxia recorded during the Late
80 Jurassic could have been caused by elevated atmospheric $p\text{CO}_2$ due to enhanced magmatic activity at
81 oceanic ridges and in subduction zones (Jones and Jenkyns, 2001; Dera et al., 2011; Meer et al., 2014;
82 Georgiev et al., 2017).

83 In the Western Tethyan domain, the Middle-Late Oxfordian interval is characterized by elevated carbon
84 isotope values from bulk carbonate ($\delta^{13}\text{C}_{\text{carb}}$) as reported by several authors (Bartolini et al., 1999; Louis-
85 Schmid et al., 2007; Rais et al., 2007; O'Dogherty et al., 2018), interpreted as the result of

86 palaeoenvironmental events (e.g., major currents reorganization, climate warming, sea-level rise, higher
87 carbonate accumulation rates). Within this overall positive $\delta^{13}\text{C}_{\text{carb}}$ interval however, during the
88 Transversarium Zone, a marked $\delta^{13}\text{C}_{\text{carb}}$ negative excursion was reported in the Jura and the Subalpine
89 Basin by Padden et al. (2001). A less well-dated negative excursion was also documented in the whole
90 Western Tethyan domain at the Middle-Late Oxfordian transition both in shallow water fossils (e.g.,
91 bivalves) and in deeper benthic organisms (e.g., belemnites; Martinez and Dera, 2015). By contrast, no
92 well-dated $\delta^{13}\text{C}$ record is available for this period in the Northern Tethys.

93 The Amu Darya Basin (ADB) is a vast sedimentary basin (*ca.* 400,000 km²) of the Northern Tethys.
94 This basin hosts the organic-rich Khodjaipak Formation, which is a major source rock for hydrocarbons
95 (Klett et al., 2006, 2012). This formation is dated from Late Oxfordian to Kimmeridgian in age
96 (Abdullaev, 2004 or Mordvintsev, 2015). These 10 to 30 m thick deposits have been identified in more
97 than two hundreds boreholes on the northeastern margin of the ADB (Besnosov and Mitta, 1995;
98 Abdullaev et al., 2010), but outcrop only at two locations in the south-west Gissar mountain range (SW
99 Gissar). In this study, field sedimentological investigations were carried out in one of these localities
100 (Tubiegatan, Uzbekistan). To date, no detailed sedimentological, mineralogical or geochemical study
101 has been published on these deposits. The Khodjaipak Fm. is located near the top of the Upper Jurassic
102 carbonates of the Kugitang Series, and could have accumulated in depressions surrounding reefal
103 buildups formed on the contemporaneous carbonate platforms (Mirkamalov et al., 2005). However, the
104 absence of outcrops between the organic deposits and their potential stratigraphic counterparts in the
105 SW Gissar implies a re-evaluation of the platform to basin correlations. The presence of ammonites in
106 the Tubiegatan section however allows herein to specify the timing of the main paleoenvironmental
107 events occurring at this period on the northern margin of the ADB.

108 In this study, the Khodjaipak Fm. organic deposits are characterized through a transdisciplinary
109 approach including sedimentology, biostratigraphy, petrography, clay mineralogy, and organic and
110 inorganic geochemistry. Our main objectives are to (i) determine the composition and the mode of
111 formation of such organic deposits, (ii) propose a high resolution biostratigraphic and carbon isotope
112 stratigraphic framework for the Tubiegatan section and (iii) establish the stratigraphic relationships with
113 the contemporaneous carbonate platform in order to specify the depositional conditions of the

114 Khodjaipak Fm. The resulting model will be compared to similar Upper Jurassic deposits worldwide in
115 order to determine potential common patterns in their formation and the potential impact on carbon
116 cycle of multiple organic carbon accumulations.

117 2. GEOLOGICAL SETTING

118 The Kugitang Series is a thick carbonate platform succession (~100–600 m) deposited on the NE
119 margins of the ADB (**Fig. 1A**) from the Early Callovian up to the Kimmeridgian (Mirkamalov et al.,
120 2005; Nugmanov, 2010; Carmeille et al., 2018). This series crops out in the southwestern Gissar
121 mountain range (SW Gissar), in the northeastern part of the ADB. The Kugitang carbonate platform is
122 subdivided into two major depositional sequences: (i) the Callovian Sequence (CS) equivalent to the
123 Lower Kugitang Series and (ii) the Upper Jurassic Sequence (UJS) equivalent to the Upper Kugitang
124 series (**Fig. 2**; Carmeille et al., 2018). The CS deposition begun in the Early Callovian and lasted at least
125 until the top of the Middle Callovian (Coronatum Zone), or possibly until the Late Callovian (**Fig. 2**;
126 Mitta, 1992). At this time, the SW Gissar was covered by a carbonate ramp. The CS ended with a major
127 subaerial exposure surface probably associated with a hiatus. The UJS records a major reorganization
128 of the platform. A vast low energy lagoon developed, probably protected by a barrier reef outcropping
129 in the Kugitang area (southern part of the SW Gissar; **Fig. 1A,B**). The organic-rich deposits of the
130 Khodjaipak Fm. could be partly time-equivalent of this barrier reef (Abdullaev, 2004). The Khodjaipak
131 Fm. dated as Upper Oxfordian and Kimmeridgian (Abdullaev, 1999, 2004; Abdullaev and Mirkamalov,
132 2001) is considered as a major type-II kerogen source rock (Ulmishek, 2004). On the Chardzhou step
133 (NE margin of the ADB; **Fig. 1A**), more than two hundred boreholes from major gas fields have drilled
134 this formation (e.g., North Kamashi, South Alan, Ayzovat 7; Ulmishek, 2004; Mirkamalov et al., 2005;
135 Abdullaev et al., 2010; Mordvintsev, 2015).

136 The Khodjaipak Fm. crops out only in two localities close to the Turkmenistan-Uzbekistan border:
137 Tubiegatan and Gaurdak (Besnosov & Mitta, 1995; **Fig. 1B**). We did not obtain authorizations to work
138 on the Gaurdak section, located on the Turkmen side. The focus of this study is the Tubiegatan section,
139 located on the Uzbek side. The section exposes a 30-meter-thick limestone interval belonging to the
140 Kugitang Series (**Fig. 2**), overlain by 10 meters of dark limestone and marl alternation (**Fig. 1C**). The

141 studied deposits crops out along a *ca.* 1 km wide window on the flank of an anticline, thanks to a local
142 gliding of the **overlying Irgayli Fm. gypsum (Figs 1D and 2).**

143 **3. MATERIALS AND METHODS**

144 **3.1. Ammonite biostratigraphy and sequence stratigraphy**

145 A total of 14 ammonites (entire or fragments) were collected **along the measured section.** Six of them
146 were determined to the species level by one of us (RE) using the standard biozonation of the NW
147 Tethyan domain (Cariou and Hantzpergue, 1997). A sequence stratigraphic scheme was built based on
148 Maximum Flooding Surfaces (MFSS) and Maximum Regressive Surfaces or Sequence Boundaries
149 (SBs), following the terminology of Catuneanu et al. (2011).

150 **3.2. Petrography**

151 A total of 90 samples were collected. To obtain a high-resolution record, one sample was taken every
152 20 cm on average within the organic-rich carbonates and marls deposits. In the limestone interval
153 (Kugitang Series), we took one sample every 1 m on average. Thin sections were prepared (polished
154 with 0.25 µm alumina powder and impregnated with blue epoxy resin) and observed under a Nikon
155 Eclipse Ci polarizing microscope for 50 samples allowing the characterization of microfacies. Three
156 thin sections were examined with a FEI Quanta 250 FEG environmental scanning electron microscope,
157 under low vacuum. One third of each thin section was etched in 10% acetic acid for 1 minute, in order
158 to remove carbonates and have a better observation of the OM. X-ray spectral microanalyses and X-ray
159 maps were performed using energy dispersive spectrometry (EDS, EDAX Apollo XL) at the I2M
160 laboratory, Bordeaux, France.

161 **3.3. Palynofacies analyses**

162 Determination of palynofacies have been realized on 28 samples. One sample (12-E1) was almost barren
163 of OM and thus unsuitable for palynofacies examination. The carbonate minerals were first dissolved
164 using hydrochloric acid (HCl). Then, the residues were treated with hydrofluoric acid (HF) in order to
165 eliminate the silicates. For each sample, two aliquots of the remaining organic residues were used to

166 make a non-filtered slide and a filtered slide using a 10 μm sieve mesh. The slides were then examined
167 under an Axioplan2 Imaging Zeiss microscope. Both qualitative and quantitative observations were
168 made. We used a simplified version of the palynofacies classifications proposed by Whitaker et al.
169 (1992) and Tyson (2012), with some modifications by McArthur et al. (2016). The relative surface area
170 of each classes was estimated on the filtered slides, as they allow a better observation of the relative
171 proportions of phytoclasts and palynomorphs. Further details regarding the palynofacies method used
172 in this study can be found in Schnyder et al. (2017). These analyses were conducted at the Institut des
173 Sciences de la Terre de Paris (ISTeP) laboratory (Sorbonne-Université, Paris, France).

174 **3.4. X-ray diffraction**

175 X-ray diffraction analyses were performed at the Biogéosciences laboratory (Université Bourgogne
176 Franche-Comté, Dijon, France) to identify and semi-quantify mineralogy of the bulk-rock (85 samples)
177 and the $<2\mu\text{m}$ clay-size fraction (80 samples). Clay minerals were identified in oriented mounts of non-
178 calcareous clay-size fraction, following the analytical procedure of Moore and Reynolds (1989). After
179 removing carbonate (using 2N HCl for marl and 12N HCl for limestone), clays were deflocculated by
180 successive washing with distilled water. Particles finer than 2 μm were concentrated by centrifugation.
181 Diffractograms were obtained using a Bruker D4 Endeavor diffractometer with $\text{CuK}\alpha$ radiation,
182 LynxEye detector and Ni filter, under 40 kV voltage and 25 mA intensity. Three XRD runs were
183 performed, after air drying (AD), ethylene-glycol solvation (EG), and heating at 490 $^{\circ}\text{C}$ for 2 h. The
184 goniometer performed a scan from 2.5 $^{\circ}$ to 28.5 $^{\circ}$ 2θ for each run. Identification and semi-quantitative
185 estimates of clay mineralogy were made according to the position and the area of the (001) basal
186 reflections on the three XRD pattern (Moore and Reynolds, 1989). The identified clay minerals are R1
187 type illite/smectite mixed-layers (I/S-R1), illite, kaolinite and chlorite. Deconvolution of peak areas of
188 kaolinite (d_{002}) and chlorite (d_{004}) was performed to discriminate both minerals using MacDiff 4.2.5
189 software (Petschick, 2001). Other non-clay minerals found in the bulk rock are calcite, quartz, feldspars
190 and pyrite. Semi-quantification of these phases are performed considering mean reflexions (100%
191 intensity) of each phase and using the $\%\text{CaCO}_3$ measured by spectrometry.

192 **3.5. Rock-Eval pyrolysis**

193 A total of 61 samples were analyzed by Rock-Eval pyrolysis using a Rock-Eval 6 Turbo (Vinci
194 Technologies) at the Institut des Sciences de la Terre de Paris (ISTeP) laboratory (Sorbonne-Université,
195 Paris, France). The following parameters were obtained (Espitalié et al., 1985; Behar et al., 2001): (i)
196 the total organic carbon (TOC, in wt %); (ii) the hydrogen index (HI, in mgHC/g-TOC), calculated from
197 the quantity of pyrolysable organic compounds from S2 peak released during pyrolysis, normalized to
198 TOC values; (iii) the oxygen index (OI, in mgCO₂/g-TOC), obtained from the amounts of CO and CO₂
199 from S3 peak released during pyrolysis, normalized to TOC values, and (iv) the T_{max}, corresponding to
200 the temperature recorded in the oven at the peak of hydrocarbon production during pyrolysis. Analytical
201 precision is ± 0.1% for TOC, ± 10 mgHC/g-TOC for HI, ± 5 mg CO₂/g-TOC for OI and ± 2°C for T_{max}.

202 **3.6. Stable isotope geochemistry ($\delta^{13}\text{C}_{\text{carb}}$, $\delta^{18}\text{O}_{\text{carb}}$, $\delta^{13}\text{C}_{\text{org}}$, $\delta^{15}\text{N}_{\text{tot}}$)**

203 The $\delta^{13}\text{C}_{\text{carb}}$ and the $\delta^{18}\text{O}_{\text{carb}}$ (bulk carbonate fraction) were measured on 72 samples at the
204 Biogéosciences laboratory (Université Bourgogne Franche-Comté, Dijon, France). About 50-90 µg of
205 powder were produced by using a micro-drill to avoid crack fillings or fossils. Powder was oven-dried
206 for 12 h at 50 °C then weighed with a Mettler Toledo XS3DU ultra-balance (30 to 60 µg, depending on
207 %CaCO₃). A Kiel IV carbonate preparation device, paired with a Delta V Plus (ThermoFisher) mass
208 spectrometer was used for isotopic analyses. Samples were dissolved at 70 °C by orthophosphoric acid,
209 and isotopic values were calibrated by NBS-19 and Merck standard. Carbon isotopic composition is
210 expressed in per mil (‰) V-PDB, and oxygen isotopic composition in ‰ SMOW. Replicates (every 7
211 samples) showed reproducibility of ± 0.07 ‰ for carbon and ± 0.1 ‰ for oxygen.

212 The $\delta^{13}\text{C}_{\text{org}}$ was measured on 75 samples and the $\delta^{15}\text{N}_{\text{tot}}$ was measured on 66 samples at the
213 Biogéosciences laboratory (Université Bourgogne Franche-Comté, Dijon, France). After grinding, the
214 carbonate minerals were dissolved using 6N HCl. The powder was then rinsed with purified water and
215 oven-dried at 50°C before analyses. The $\delta^{13}\text{C}_{\text{org}}$ and $\delta^{15}\text{N}_{\text{tot}}$ analyses were performed using a vario
216 MICRO cube (Elementar) elemental analyser, paired to an Isoprime (Elementar) isotope ratio mass
217 spectrometer (EA-IRMS). The values were compared to USGS40 L-Glutamic acid ($\delta^{13}\text{C} = -26.39 \pm 0.04$
218 ‰; $\delta^{15}\text{N} = -4.5 \pm 0.1$ ‰) and IAEA-600 Caffeine ($\delta^{13}\text{C} = -27.77 \pm 0.04$ ‰; $\delta^{15}\text{N} = +1.0 \pm 0.2$ ‰)

219 international standards for $\delta^{13}\text{C}_{\text{org}}$ and $\delta^{15}\text{N}_{\text{tot}}$. The $\delta^{13}\text{C}_{\text{org}}$ and $\delta^{15}\text{N}_{\text{tot}}$ values are expressed in ‰ V-PDB
220 and ‰ V-AIR respectively. For each sample, replicates showed reproducibility better than ± 0.3 ‰ for
221 $\delta^{13}\text{C}$ and ± 0.5 ‰ for $\delta^{15}\text{N}$.

222 **3.7. Major and trace element geochemistry**

223 Multi-elemental analyses were performed using ICP-AES for major elements and ICP-MS for trace
224 elements on 23 samples at the spectrochemical laboratory of the Centre de Recherche Pétrographiques
225 et Géochimiques (CRPG, Vandoeuvre-les-Nancy, France). The samples were prepared by fusion with
226 LiBO_2 and HNO_3 dissolution. The average uncertainties are about 1% for major elements, 5% for Cr, U
227 and V, and 10% for Co, Mo, and Ni as checked by international standards (Carignan et al., 2001).

228 Usually, trace elements are Al-normalized in order to dissociate the detrital and authigenic fractions.
229 However, because of fluctuating Al concentrations (from 0.08 to 5%), the use of fraction in excess was
230 preferred to dissociate these two fractions. As proposed by Brumsack (2006), the detrital fraction X_{detritic}
231 has been calculated using the formulae: $X_{\text{detritic}} = \text{Al}_{\text{sample}} \times (X/\text{Al}_{\text{upper crust}})$. The values of upper **continental**
232 crust are from McLennan (2001). Then, the “excess” (non-detrital) fraction has been calculated, using
233 the formulae $X_{\text{xs}} = X_{\text{sample}} - X_{\text{detritic}}$ for each element, which does not show strong correlations with Al
234 and Ti, considered as elements with a detrital origin (Tribovillard et al., 2006; Collin et al., 2015).

235 **4. RESULTS AND INTERPRETATIONS**

236 Based on the vertical facies succession, we defined three lithostratigraphic intervals along the
237 Tubiegatan section: (1) a lower carbonate interval; (2) an organic-rich marl and limestone unit
238 corresponding to the Khodjaipak Fm. and (3) a second carbonate interval at the top. In terms of sequence
239 stratigraphy, the whole succession can be interpreted as a transgressive-regressive third-order sequence
240 with a proposed MFS located *ca.* 20 m from the basis of the section. This sequence can be subdivided
241 into three higher frequency depositional sequences (Tu1, Tu2 and Tu3; **Fig. 3**).

242 **4.1. Sedimentology and stratigraphy**

243 **4.1.1. Lower carbonate interval (0–30 m), Tu1 and Tu2 sequences, base of Tu3 sequence**

244 Mudstones (F2a) and pellet-sponge spicule wackestones (F2b) predominate in the first 25 meters of the
245 section (**Fig. 3**). Such mud and pellet-rich facies are indicative of low energy conditions (Carmeille et
246 al., 2018), and in the absence of storm-deposits they are usually placed below the storm wave base
247 (SWB; Wilson, 1975; Carpentier et al., 2007). The diversified photo-independent benthic associations:
248 sponge spicules, benthic foraminifera, echinoderms and oysters, suggest a well-oxygenated bottom
249 water located below the photic zone. Ammonite imprints were also locally observed at the surface of
250 beds. The micritized ooids (F2e) observed at 14 and 29 m could be exported from the inner platform
251 during shallowing-upward trends. Dolomitized *Thalassinoides* burrowed horizons (**Fig. 4B,C**) reflect
252 the formation of firmgrounds possibly recording a decrease in the sedimentation rate and water depth
253 (Carmeille et al., 2018). Consequently, we placed two 4th order sequence boundaries (14 m and 27 m)
254 within these burrowed intervals (**Fig. 3**). The occurrence of *Perisphinctes* (*Kranaosphinctes*) sp. would
255 place the top of Tu1 and the basis of Tu2 in the Oxfordian. The dolomitized *Thalassinoides* burrows at
256 the top of Tu2 (25 to 27 m) are locally filled with diagenetic iron oxides.

257 The overlying carbonate strata (27 to 30 m) are characterized by serpulids and benthic foraminifera
258 (including Lituolids) packstone (F2c) and *Crescentiella morronensis* and brown foraminifera oncoids
259 pack- to floatstone (F2d). They are placed within the sequence Tu3. The last bed of the lower carbonate
260 interval shows a significant fossil concentration: ammonites, belemnite rostra, oysters and benthic
261 foraminifera (F1d). This fossil association indicates the persistence of a good oxygenation of the whole
262 water column. A hardground develops at the top of this bed, likely reflecting a decreased sedimentation
263 rate. Overall, the lower carbonate interval was mostly deposited below SWB and shows evidence for a
264 well-oxygenated water column.

265

266 **4.1.2. The Khodjaipak Fm. (30–40 m), Tu3 sequence**

267 From 30 to 40 m (**Fig. 3**), the series is dominated by organic-rich marls to siltstones (F1a) and microbial
268 boundstones (F1c), interbedded with black nodular mudstones (F1b) and tempestites (F1d). Millimeter-

269 laminated dark to brown marls to siltstones (F1a; **Fig. 4D**) containing ammonites and entire bivalves in
270 life position are characterized by TOC values comprised between 0.4% and 4%. The black nodules (F1b)
271 found in these dark to brown marls show the highest TOC values, reaching 6% (**Fig. 4E**). F1c consists
272 of sub-millimetric alternations of carbonate and organic laminae (**Fig. 5A-C**), with TOC values
273 comprised between 0.5% and ~2% (**Fig. 3**). Sponge spicules, benthic (rotaliids: *Lenticulina*,
274 *Rheinholdella?*) and planktonic foraminifera are locally concentrated in thin laminae (**Fig. 5D**).
275 Diagenetic anhydrite pseudomorphs and dolomite rhombs are observed in this facies (**Fig. 5B**). F1d
276 corresponds to dark shell beds (**Fig. 4F**) with moderate TOC (0.8-1.6%). The skeletal elements consist
277 of well-preserved, disarticulated and oriented brachiopod and bivalve shells (e.g., *Trichites*, pectinids,
278 oysters), which are associated with abundant rotaliid foraminifera (identical to those observed in F2c),
279 sponge spicules and rare echinoderm fragments floating in a dark-micritic matrix. The ammonite
280 *Subdiscosphinctes (Subdiscophinctes) cf. richei* De Riaz /*mindowe* Siemiradzki precisely dates this
281 interval to the Schilli Subzone (Transversarium Zone, Middle Oxfordian; **Fig. 3**). **The suggested**
282 **depositional environment for these organic carbonates is discussed in details in Section 5.3.1.**

283 **4.1.3. Upper carbonate interval and chicken wire gypsum (40–43m), Tu3 sequence**

284 The section is capped by a 2-m-thick carbonates interval characterized by peloid and fine micritized
285 ooid pack- to grainstone (F3a) and stromatolitic boundstone (F3b). These carbonates are overlain by
286 chicken-wire gypsum, typical of sabkha deposits, whose exact thickness cannot be determined (F4; **Fig.**
287 **3**).

288 **4.2. Petrography of microbial organic carbonates**

289 The organic-rich, laminated microbial boundstone (F1c; **Fig. 5A,B**) is abundant in the Khodjaipak Fm.
290 (**Fig. 3**). This facies displays two main microfabrics: (i) 10 µm to 1 mm thick organic and
291 micritic/microsparitic laminae that alternate with (ii) 100s of microns to 3 mm thick peloidal laminae
292 (**Fig. 5C**). Macroscopically (**Fig. 5A**), the carbonate-rich beige laminae and the dark organic-rich
293 laminae alternation are very similar to the intertidal microbial mats observed in the modern Abu Dhabi
294 sabkha (Lokier et al., 2017). Microspar and micrite are abundant in both dark and clear laminae (**Fig.**
295 **5E**). Foraminifera (**Fig. 5D**) and sponge spicules rich laminae were probably formed through trapping

296 and binding processes (e.g., Bouton et al., 2016). OM has two main loci: (i) yellowish to dark aggregates
297 are observed within peloids (**Fig. 5C**) and microspar crystals (**Fig. 5F**); similar coccoid bacteria clusters
298 are documented in modern hypersaline lagoon microbialites (e.g., Dupraz et al., 2004); (ii) a thin dark
299 lining occurs between spar crystals (**Fig. 5E,F**) and sometimes impregnates the wall of foraminifera and
300 other microfossils (**Fig. 5D**). Three samples were observed under SEM and analysed with EDS (**Fig. 6**).
301 Peloids develop within an alveolar OM network (**Fig. 6A-C**), very close to modern microbial mats
302 exopolymeric substances (EPS; e.g., Dupraz et al., 2004; Pace et al., 2018). Platy clay minerals
303 characterized by high content in Al, and possibly of detrital origin, are associated with OM (**Fig. 6D**).
304 The clay-OM complexes include very small sulfur globules (mostly <1µm in diameter). Some samples
305 show a significant proportion of iron oxides associated with organic carbon (**Fig. 6E,F**).

306 **4.3. Bulk and clay mineralogy**

307 Carbonates predominate in the lower and upper carbonate intervals (90-100% of CaCO₃; **Fig. 3**). In the
308 Khodjaipak Fm., the proportion of calcium carbonate and quartz fluctuates: microbial laminites (F1c)
309 contain up to 92% of CaCO₃, while brown marls to siltstones contain up to 50% of quartz. The
310 proportion of clay minerals in the bulk rock is overall low (< 1%) in the lower and upper carbonate
311 intervals. The percentage increases in the Khodjaipak Fm., where clay accounts for up to 8% of the bulk
312 rock. Pyrite content is relatively low (< 0.5%) in the lower and upper carbonate intervals and reaches
313 1% for several horizons within the Khodjaipak Fm. (**Fig. 3**).

314 We subdivide the section into five intervals based on the clay mineral association (intervals 1 to 5; **Fig.**
315 **3**). From 1 m to 20 m, the relative percentage of the various clay minerals is relatively constant: illite
316 predominates with values comprised between 55 and 75%, followed by R1 type illite/smectite mixed-
317 layers (I/S-R1; 20-40%), kaolinite (0-10%) and chlorite (0-5%). A second interval (20 to 30 m) is
318 characterized by an increase of kaolinite (up to 40% at 27.5 m) followed by a slight decrease, at the
319 expense of illite (approximately 40 to 70%). Chlorite displays similar variations as kaolinite, but
320 represents a smaller proportion of the clay assemblage (< 15%). I/S-R1 content ranges between 15 and
321 25%. The third interval (30 to 36 m), starting at the basis of the Khodjaipak Fm., is marked by highest
322 content and significant fluctuations of kaolinite, with two peaks at 31 and 31.7 m, reaching 65% and

323 63% respectively, and the decrease of illite and chlorite contents. From 36 m to 40 m (interval 4),
324 kaolinite and chlorite are absent, IS-R1 varies between 0 and 30%, while illite remains the dominant
325 clay mineral.

326 **4.4. Rock Eval pyrolysis**

327 TOC values range from 0wt% (peloidal pack- to μ grainstone, F3a) to 6wt% for the thinly laminated
328 black limestones with nodules (F1b; **Figs 3 and S1**). The lower carbonate interval does not contain
329 organic carbon. Within the Khodjaipak Fm., the higher TOC values were measured in limestones (2.0%
330 on average in F1b, F1c and F1d) while lower TOC values (avg. 0.5%) characterized marls and claystone
331 (F1a; **Fig. S1**). The TOC is relatively low (0-1.8%) from 30 to 33.5 m, then increases from 33.5 to 34.5
332 m and remains at fluctuating but relatively high values (0.7-6%) up to 38 m to finally progressively
333 decrease to 0% in the upper carbonate interval.

334 Throughout the dark organic-rich deposits interval, the T_{max} values form two groups (**Fig. 7**). Most of
335 the values range between 440 and 465°C, characterizing a mature OM which has reached the oil
336 window, while a second group shows values comprised between 515 and 540°C (**Fig. 7**), indicating the
337 gas window (Tyson, 1995). The HI values obtained in the Khodjaipak Fm. range from 7 to 142 mgHC/g-
338 TOC. Along the studied section, the HI fluctuates rapidly between values above 100 mgHC/g-TOC and
339 below 50 mgHC/g-TOC (**Fig. 7**). These observations as well as the high values of T_{max} may be the
340 reflection of a degradation of the OM. The HI / T_{max} relation (**Fig. 7**) points to a Type III (terrestrial
341 OM) to Type IV OM, the latter characterizing a highly altered organic material (generally oxidized)
342 whose biological origin is not determinable (Baudin et al., 2007). However the burial of OM selectively
343 removes hydrogen-rich OM and induces a depletion of IH values (Espitalié et al., 1985). Consequently,
344 it is probable that at least a part of the OM was originally of Type II (marine OM) and was subsequently
345 thermally degraded. Therefore, the Rock-Eval analysis is most probably not conclusive regarding the
346 OM origin, and palynofacies data are used to discriminate OM sources (see section 4.5).

4.5. Palynofacies

The studied palynofacies comprise nine classes of components (**Fig. 8**), following a simplified version of the palynofacies classifications published by Whitaker et al. (1992), Tyson (1995) and McArthur et al. (2016): (i) opaque phytoclasts, (ii) translucent phytoclasts, (iii) dark structureless organic matter (DSOM), (iv) well-preserved wood fragments (WPWF), (v) amorphised degraded brown wood (DBW) and dark amorphous organic matter (AOM) flakes with rectangular shapes, (vi) pollen grains and spores, (vii) orange to dark AOM flakes, (viii), dinoflagellate cysts, and (ix) foraminiferal linings. The translucent phytoclasts correspond to flat, pale brown to transparent fragments including leaf cuticles and aqueous plant remains. DSOM are dark brown to orange fragments originating from degraded products of plant debris and humic gel. WPWF are dark-brown fragments showing preserved wood structures (tracheids, lignified walls). DBW and rectangular AOM are dark-brown to yellow, flat, with gelified to amorphized structures. These particles partly derive from terrestrial wood fragments and/or from lignified parts of aqueous plants that are heavily degraded, gelified and amorphized in an aqueous environment. Similar amorphization and gelification processes due to bio-degradation of terrestrial or aquatic plant tissues have been reported in peat and aquatic marshes environments (Laggoun-Défarge et al., 1999; Sebag et al., 2006; Storme et al. 2012). The vertical evolution of the relative percentage of these classes is represented on **Figure 8**.

AOM is largely predominant in the Tubiegatan section, accounting for more than 75% in the countings in 18 out of 27 samples (**Fig. 8**). AOM is generally interpreted as being of microbial and/or algal origin (e.g., Tyson, 1995) and a mostly marine origin of the AOM is probable in the Tubiegatan section. However, dark AOM particles with rectangular shape observed at some stratigraphic levels between 34.8 and 38.8 m are associated with DBW. Therefore, this type of AOM **could be** different from the rest of the observed AOM, and is here interpreted as most probably originating from degraded terrestrial and/or aquatic macrophytes tissues. A second characteristic of the palynofacies from Tubiegatan is the common occurrence of -at least partly- terrestrial-derived materials, such as opaque and translucent phytoclasts, DSOM, WPWF, amorphised DBW, and pollen and spores. This could be related to the proximity of emerged lands or islands and the relative shallowness of the sea (Carneille et al., 2018).

374 The Tubiegatan section can be subdivided into four palynofacies intervals, from base to top (**Fig. 8**):

375 -Interval I (8.4 to 27 m) is characterized by elevated proportions of small size translucent phytoclast
376 fragments, generally > 50%, low proportions of AOM and a small fraction of opaque phytoclasts. Pollen
377 and spores, dinoflagellate cysts and foraminiferal linings occur in traces. Interval I coincides with the
378 top of the sequence Tu1 and the sequence Tu2 (**Fig. 8**). The large proportions of translucent phytoclasts
379 such as cuticles and the local influx of wood fragments (opaque phytoclasts) indicate the proximity of
380 emerged lands.

381 -Interval II (27 to 33.9 m) presents high proportions of AOM (> 90%), and
382 minor proportions of translucent phytoclasts. Amorphized DBW, opaque
383 phytoclasts, DSOM, WPWF, pollen and spores, dinoflagellate cysts and
384 foraminiferal linings occur in traces. This interval corresponds to the
385 basal part of the Khodjaipak Fm., which shows low to moderate amount of
386 preserved OM (TOC ≤2%, TOC=0.86 % on average; **Fig. 8**).

387 -Interval III (33.9 to 39.6 m) shows alternatively predominant proportions (> 85%) of AOM and
388 amorphized DBW and rectangular AOM flakes. Minor proportions of opaque phytoclasts occur between
389 38 and 38.8m. DSOM, WPWF, pollen and spores, dinoflagellate cysts and foraminiferal linings occur
390 in traces. Interval III is associated with the upper part of the Khodjaipak Fm., which shows enhanced
391 accumulation of OM (TOC up to 6%, TOC=1.8% on average; **Fig. 8**).

392 -Interval IV (39.6 to 41 m) shows a predominance of AOM, however with lower proportions than within
393 Interval III (AOM=61-79.7%), and moderate proportions (11.4-16%) of translucent phytoclasts. Opaque
394 phytoclasts, pollen and spores, dinoflagellate cysts and foraminiferal linings occur in traces. It should
395 be highlighted that the palynomorphs are not well-preserved and it is somewhat difficult to identify
396 dinoflagellate cysts properly, especially in sample 09-E16 at 40 m. Palynofacies results from this sample
397 should thus be taken with caution. Interval IV corresponds to the Upper carbonate interval of the
398 Tubiegatan section, which shows low accumulation of OM (TOC=0.2% on average; **Fig. 8**).

399 **4.6. Stable isotope signals and C/N records**

400 **Figure 9** presents the vertical evolution of $\delta^{13}\text{C}_{\text{carb}}$, $\delta^{18}\text{O}_{\text{carb}}$, $\delta^{13}\text{C}_{\text{org}}$ and $\delta^{15}\text{N}_{\text{tot}}$. In the lower carbonate
401 interval, the $\delta^{13}\text{C}_{\text{carb}}$ remains positive (4-4.5‰) and relatively stable up to a small negative excursion
402 (amplitude 0.3‰) at 14 m followed by a positive excursion (amplitude 0.7‰) at 20 m. The top of the
403 lower carbonate interval (20 to 30 m) and the base of the Khodjaipak Fm. (30 to 33 m) record a rapid
404 and significant decrease of $\delta^{13}\text{C}_{\text{carb}}$ (amplitude of *ca.* 4‰) to reach values close to 0. Very negative and
405 fluctuating $\delta^{13}\text{C}_{\text{carb}}$ values (avg. -2.3‰) characterize the remaining part of the Khodjaipak Fm. (33-40
406 m). An overall decrease occurs from 33 to 38 m to reach the most negative value (-10‰), which is
407 recorded in an organic microbial boundstone (F1c; **Fig. 10**). The signal then increases up to the top of
408 the Khodjaipak Fm. In the upper carbonate interval, the values progressively increase but remain below
409 1‰. Overall, black nodular mudstones and microbial boundstones have the most negative $\delta^{13}\text{C}_{\text{carb}}$
410 (respectively -4‰ and -0.7‰ on average; **Fig. 10**).

411 The $\delta^{18}\text{O}_{\text{carb}}$ signal records strong variations between 0 and 12 m (amplitude of *ca.* 4‰) then
412 progressively increases up to the top of the lower carbonate interval, with a maximum value of 0.8‰.
413 The following Khodjaipak Fm. is marked by oscillating $\delta^{18}\text{O}_{\text{carb}}$ values (avg. -3.4‰) combined with a
414 stepwise decrease up to 38 m (min.: -12‰; **Figs 9 and 10**). The top of the Khodjaipak Fm. and the
415 following upper carbonate interval are characterized by a slight $\delta^{18}\text{O}_{\text{carb}}$ increase (max: -1.4‰).

416 The $\delta^{13}\text{C}_{\text{org}}$ signal (**Fig. 9**) fluctuates slightly around -25‰ for most of the lower carbonate interval,
417 except near the top of the Tu1 sequence (9.5 to 12 m), **where the values rapidly decrease (-27.4‰) and**
418 **increase to reach their maximum (-23.4‰)**. The signal drops from 24 to 34 m, recording its lowest value
419 (-28.5‰) near the transition between the palynofacies intervals II and III. Then the signal slightly
420 increases and fluctuates between -27 and -28‰ up to the top of the Khodjaipak Fm.

421 The $\delta^{15}\text{N}_{\text{tot}}$ values are relatively stable in the lower carbonate interval (avg. 2.7‰). The Khodjaipak Fm.
422 shows overall lighter $\delta^{15}\text{N}_{\text{tot}}$ (avg. 1.7‰) with significant fluctuations, between -1.1 and 4.5‰. The
423 lowest values are recorded within the two anoxic intervals (**Fig. 9**).

424 The C/N ratio (**Fig. S3**) fluctuates between 5.5 and 81.9 (avg. 14.7) along the lower carbonate interval.
425 The variations increase in amplitude (8.6 to 187; avg. 39.2) in the Khodjaipak Fm.

426 **4.7. Major and trace elements**

427 Most of major elements (Si, Fe, K, Ti) and many trace elements (Cr, Co, Th, Pb) show strong correlation
428 ($R > 0.9$) with Al and are thus associated with the detrital fraction. Only few elements (Cd, Mo, Ni, U,
429 V, Zn) are not ($R < 0.5$) or only slightly to moderately ($R < 0.9$) correlated with Al and show noticeable
430 positive values of fraction in excess. This is particularly true for Mo, U and to a lesser extent V, which
431 are particularly sensitive to oxygen variations. An increase of their concentrations compared with the
432 upper continental crust values (1.5 ppm for Mo, 107 ppm for V and 2.8 ppm for U; McLennan, 2001)
433 point to O₂-depleted conditions (Tribovillard et al., 2006; Lézin et al., 2013). **Here, only the evolution**
434 **of Mo_{xs} will be shown and discussed, U and V having the same evolution (Fig. 11).** In the Khodjaipak
435 Fm., punctual peaks of Mo_{xs} are observed, one at 34.5 m (73.2 ppm) and two others are observed at 37.2
436 and 38.3 m (with values up to 75.3 ppm; **Fig. 11**). In the second interval, the highest values of Mo_{xs} are
437 related to the microbial boundstone (F1c).

438 To better constrain the O₂ variations, U/Th and V/Cr ratios were calculated. They are both used as
439 oxygenation tracers at the water-sediment interface or in the sediment. Based on threshold values,
440 defined by Jones and Manning (1994), these ratios allow to distinguish oxic (U/Th < 0.75 and V/Cr $<$
441 2.00), dysoxic and anoxic (U/Th > 1.25 and V/Cr > 4.25) conditions. In the Khodjaipak Fm., the values
442 of ratios range from 0.95 to 8.00 for U/Th and from 1.40 to 13.40 for V/Cr (**Fig. 11**), indicating O₂-
443 depleted conditions. Two intervals are characterized by high values of these ratios attesting for anoxic
444 conditions: the AI1 (for Anoxic Interval n°1) extends from 33.4 to 35.0 m, the AI2 from 37.0 to 38.7 m
445 (**Fig. 11**). The two anoxic intervals coincide with most of the elevated TOC values. The lower values
446 below AI1, between AI1 and AI2 and above AI2 reflect dysoxic conditions.

447 5. DISCUSSION

448 5.1. Signal preservation and signification

449 5.1.1. Organic matter

450 The T_{\max} from Rock-Eval analyses indicate the influence of a burial diagenesis consistent with the oil
451 window (**Fig. 7**). The HI and OI values plotted in the Van Krevelen diagram (**Fig. S2**) suggest the
452 presence of altered OM (Type IV) and/or continental (Type III) OM. Nevertheless, in the case of thermal
453 diagenesis associated with marked burial of the sediments, the hydrogen bonds of organic molecules are
454 particularly affected, leading to a decrease of the original HI values (Espitalié et al., 1985). HI values
455 were thus originally higher than recorded, probably mostly fitting with a Type II (marine) OM, as
456 reflected by predominant AOM in palynofacies. **Furthermore, the local presence of orange-colored**
457 **AOM, combined with a relatively low amount of pyrite (< 2%) could reflect an early diagenetic**
458 **sulfurization of OM (Tribovillard et al., 2004). This process is widespread in anoxic marine environment**
459 **and implies reactions between dissolved sulfide species and energy-rich moieties in the OM (e.g.,**
460 **alcohols, aldehydes). Sulfurized polymers (mostly lipids) are more resistant to microbial and/or thermal**
461 **degradation (Raven et al., 2019), which could explain the preservation of substantial amounts of OM in**
462 **the Khodjaipak Fm.** The low OI values (**Fig. S2**) also suggest that most of the OM of the Khodjaipak
463 Fm. is a thermally degraded Type II OM (Espitalié et al., 1985; Tyson, 1995). Accordingly, the
464 measured TOC values are lower than the original ones. As TOC values reach up to ~6% in the
465 Khodjaipak Fm., this implies high to very high original OM accumulation for a marine depositional
466 environment. Despite a significant burial, the consistency of palynofacies, organic carbon geochemistry
467 and sedimentary facies indicates that the OM retains part of the paleoenvironmental signal.

468 5.1.2. Clay minerals

469 The presence of kaolinite is compatible with limited burial temperatures, probably less than 160°C
470 (Sucha et al., 1993). Dellisanti et al. (2010) estimated that for T_{\max} ranging from 434 to 465°C, the
471 content of illite in the IS-R1 should vary between 60 and 85%. In this context the illitization of potential
472 former smectites or smectite-rich interstratified clay mineral such as IS-R0 may have occurred, these
473 transformations taking place around 80-100°C, i.e. from 2 to 3 km of burial for a normal geothermal

474 gradient (Chamley, 1989). Both clay mineral assemblages and the maturity of the OM agree therefore
475 with a minimal burial depth of *ca.* 2-3 km for the Khodjaipak Fm., if we consider a normal geothermal
476 gradient. Occurrence of initial smectite-rich clay minerals in the initial sediment is therefore a possibility
477 and could correspond to current IS-R1. Preservation of kaolinite less sensitive to burial diagenesis allows
478 to use these detrital clay minerals for palaeoclimate reconstruction, as no evidence of clay mineral
479 authigenesis was recognized.

480 **5.1.3. Carbonates**

481 The petrographic examination of the lower carbonate interval and of the Khodjaipak Fm. deposits points
482 to moderate chemical and/or mineralogical diagenetic transformations. The predominantly micritic
483 facies of the lower carbonate interval show very small quantities of carbonate cements, except for late
484 fracturation (e.g., **Fig. 4B**). The Khodjaipak Fm. is also cross-cut by late fractures infilled with fibrous
485 gypsum, possibly formed through precipitation of sulfate-rich fluids coming from the overlying sabkha
486 gypsum (**Irgayli Fm.; Fig. 3**). Microbial facies are predominantly micritic to microsparitic (**Fig. 6**). This
487 probably indicates a moderate cementation and recrystallization of the carbonate minerals. The negative
488 $\delta^{18}\text{O}_{\text{carb}}$ values comprised between 1‰ to -5‰ with two values reaching -8‰ and -12‰ (**Figs 9, 10**)
489 indicate a potential contribution of meteoric water. However, in modern microbialites, the micrite to
490 microspar transition can take place in the depositional environment. It is not necessarily related to
491 meteoric cementation, but can also result from physico-chemical precipitation in alkaline water close to
492 the microbialite surface, though the resulting isotopic values are generally not very negative (Dupraz et
493 al., 2004, 2013). By contrast, the upper carbonate interval shows an intense cementation and a poor
494 preservation of the facies, which indicates a probable strong diagenetic influence.

495 The effects of recrystallization by fluids circulation could affect the isotopic signal, particularly the
496 $\delta^{18}\text{O}_{\text{carb}}$ primary signal, which is more sensitive than the $\delta^{13}\text{C}_{\text{carb}}$ (Immenhauser et al., 2002; Louis-
497 Schmid et al., 2007). A strong covariation of $\delta^{13}\text{C}_{\text{carb}}$ and $\delta^{18}\text{O}_{\text{carb}}$ usually indicates the influence of
498 meteoric fluids (e.g., Marshall, 1992). **Figure 10** presents a $\delta^{13}\text{C}_{\text{carb}}$ vs. $\delta^{18}\text{O}_{\text{carb}}$ cross plot. The linear
499 least square regressions were calculated for the lower carbonate interval ($R^2 = 0.3$, P-value < 0.05) and

500 the Khodjaipak Fm. ($R^2 = 0.3$, P-value < 0.05). The results confirm a possible significant diagenetic
501 imprint on the $\delta^{18}\text{O}_{\text{carb}}$, which is consequently not used for palaeoclimate reconstructions.

502 **5.1.4. Sulfides and iron oxides**

503 Given their morphology and their association with OM-clay complexes, the very small sulfur-rich
504 globules (< 1 μm in diameter) that are observed in microbial boundstones (**Fig. 6D**) are likely of
505 microbial origin. They are very similar to the globules produced by sulfide-oxidizing anoxygenic
506 phototrophic bacteria in modern hypersaline microbial mats (e.g., Pace et al., 2018). The Khodjaipak
507 Fm. also shows moderate amounts of pyrite (< 1.5% of the bulk sediment) decreasing upward (**Fig. 3**).
508 Pyrite is a common byproduct of microbial sulfate reduction and is common in organic-rich sedimentary
509 formations (e.g., Rickard et al., 2017; Raven et al., 2019). **The relatively low proportions of pyrite**
510 **characterized here could be the result of the competition between reactive sulfides and OM for reactive**
511 **Fe shortly after deposition (Shawar et al., 2018). A significant OM production, as postulated for the**
512 **Khodjaipak Fm., could constitute a Fe sink and prevent pyrite precipitation (see section 5.3.3).** At the
513 micro-scale, the Fe oxides locally associated with OM (**Fig. 6F**) could derive from the oxidation of
514 pyrite originally associated to OM-clay complexes. Fibrous gypsum **filling fractures** testifies of the **post-**
515 **depositional** circulation of sulfate-rich fluids in the rock. These oxidizing fluids, probably coming from
516 the overlying gypsum deposits (Irgayli Fm.; **Fig. 2**), could have induced the oxidation of primary pyrite.
517 Overall, the top of the Khodjaipak Fm. is more affected by the circulation of oxidizing, probably saline
518 fluids than its base.

519 **5.2. Age of the Khodjaipak Fm. and stratigraphic relationship with the SW Gissar** 520 **carbonate platform**

521 Based on ammonite biostratigraphy, Abdullaev (2004) dated the Khodjaipak Fm. as Late Oxfordian to
522 Kimmeridgian, while Mitta and Besnosov (2007) suggested a Late Oxfordian to Early Kimmeridgian
523 age. The ammonite fauna **identified in this study** indicates a Middle Oxfordian age at least in Tubiegatan
524 (**Fig. 3**). *Dichotomosphinctes luciaeformis* indicates an older age for the top of the lower carbonate
525 interval (Transversarium Zone, Luciaeformis subzone), while *Subdiscosphinctes (Subdiscosphinctes)* cf.

526 *richei* De Riaz /*mindowe* Siemiradzki gives a more recent age (Transversarium zone, Schilli subzone)
527 in the upper part of the Khodjaipak Fm. The fact that all these deposits belong to two successive
528 subzones also indicates that there is no major stratigraphic hiatus associated with the hardground at the
529 top of the lower carbonate interval (Fig. 3).

530 A vast carbonate platform developed over the SW Gissar between the Early Callovian and potentially
531 the Kimmeridgian (Abdullaev, 2004; Nugmanov, 2010; Carmeille et al., 2018). Carmeille et al. (2018)
532 subdivided the platform succession in two major sequences: (i) a ramp developed during the Callovian
533 Sequence (CS; equivalent to the Lower Kugitang Fm. of Nugmanov, 2010), which is dated as Early-
534 Middle Callovian with ammonites, and possibly includes Upper Callovian deposits; (ii) The Upper
535 Jurassic Sequence (UJS; equivalent to the Upper Kugitang Fm. of Nugmanov, 2010) develops above a
536 major sequence boundary (SB2) and after a hiatus potentially encompassing the top of the Callovian
537 and the base of the Oxfordian (Fig. 2). In the SW Gissar, the UJS is dominated by mud or oncoid-rich
538 lagoonal deposits (the Gardarin Fm. of Abdullaev et al., 2010) passing southward to ooid shoal
539 grainstones and peri-reefal facies. Carmeille et al. (2018) proposed a correlation between several $\delta^{13}\text{C}_{\text{carb}}$
540 excursions recorded in the UJS and the well-dated NW Tethyan bivalve $\delta^{13}\text{C}$ record compiled by Dera
541 et al. (2011). This correlation would date the UJS as Early to Late Oxfordian. The stratigraphic
542 relationships between the SW Gissar carbonate platform and the Khodjaipak Fm. are key to understand
543 the palaeogeographic setting and to establish a depositional model for the organic carbonates.

544 Some authors (e.g., Abdullaev, 2004; Nugmanov, 2010) propose a model where organic shales
545 (Khodjaipak Fm.) accumulate in a starved basin separated from the lagoon (Gardarin Fm.) by a large-
546 scale barrier reef (Urtabulak Fm.). Besides the presence of Oxfordian ammonite specimens recognized
547 in the Khodjaipak Fm., the lower carbonate interval of the Tubiegatan section shows heavy $\delta^{13}\text{C}_{\text{carb}}$
548 values (4.25‰ on average), which largely overlap with the values measured in the UJS lagoonal deposits
549 (4.00‰ on average; Fig. 10). Consequently, the lower carbonate interval, underlying the Khodjaipak
550 Fm. could be time equivalent of part of the UJS inner shelf deposits in the SW Gissar.

551 The UJS is subdivided into two medium-scale sequences, UJS1 and UJS2, which are separated by a
552 major sequence boundary which resulted in the exposure of the northern part of the SW Gissar platform

553 (SB3; **Fig. 12**; Carmeille et al., 2018). We propose two correlation hypotheses between the organic-rich
554 Tubiegatan succession and the SW Gissar inner platform deposits, based on the carbon-isotope signal
555 and the sequence stratigraphy.

556 **5.2.1. Hypothesis n°1**

557 The first hypothesis (**Fig. 12A**) correlates the $\delta^{13}\text{C}_{\text{carb}}$ positive peak (*ca.* 0.5-1.2‰) recorded in the
558 middle part of UJS1 in the Baglydara and Pyandzh Ob sections with a similar excursion in the lower
559 carbonate interval of the Tubiegatan section (*ca.* 0.5‰ of amplitude, **Fig. 12A**). Above, a gradual
560 decrease of $\delta^{13}\text{C}_{\text{carb}}$ is recorded up to SB3, leading to a marked negative excursion in the $\delta^{13}\text{C}_{\text{carb}}$
561 (amplitude > 0.5‰ in Baglydara, > 2‰ in Pyandzh Ob and *ca.* 1‰ in Derbent; **Fig. 12A**). The $\delta^{13}\text{C}_{\text{carb}}$
562 then progressively increases of 1.5 to 2‰ above SB3. In Tubiegatan, the $\delta^{13}\text{C}_{\text{carb}}$ shows a decrease of
563 *ca.* 4‰ encompassing the top of the lower carbonate interval and the basis of the Khodjaipak Fm. Then,
564 the values drop down to -10‰ in Khodjaipak Fm. before a progressive increase (amplitude > 10‰)
565 from the top of the Khodjaipak Fm. to the upper carbonate interval. Hypothesis n°1 implies a correlation
566 of these two negative peaks of different amplitude. In this scenario, the Khodjaipak Fm. would have
567 deposited at a period of low sedimentation rate (recorded by burrowed horizons) and partial subaerial
568 exposure of the platform associated with SB3 (Carmeille et al., 2018).

569 **5.2.2. Hypothesis n°2**

570 In the second hypothesis, we correlate the slight positive excursion recorded in Tubiegatan with three
571 similar excursions (amplitude of *ca.* 1‰) recorded in the first half of UJS2 in the SW Gissar sections
572 (blue colour, **Fig. 12B**). This is followed by rapid 1 to 1.5‰ fluctuations in the $\delta^{13}\text{C}_{\text{carb}}$ in Baglydara or
573 by 1 to 2‰ negative carbon-isotope excursions in Pyandzh Ob and Derbent, about 40–60 m under the
574 nodular gypsum strata of the SW Gissar platform (**Fig. 12B**). The same negative excursion was recorded
575 below evaporites in other SW Gissar sections (e.g., Langar; Carmeille et al., 2018). In Derbent, the top
576 of the carbonate succession shows a *ca.* 2‰ **positive excursion in the $\delta^{13}\text{C}_{\text{carb}}$ record. This excursion can**
577 **be correlated with the positive excursion recorded at the top of the Khodjaipak section.** Hypothesis n°2
578 is supported by sedimentological arguments. UJS2 displays several bioturbated horizons (e.g., in
579 Baglydara and Derbent sections). Similar burrowed limestones are also observed along the lower

580 carbonate interval in Tubiegatan, at Tu1 and Tu2 sequence boundaries (**Figs 3, 12**). In the proposed
581 correlation, the burrowed horizons would be approximately in the same stratigraphic interval as in
582 Tubiegatan. Inner platform stromatolites and pellet-rich deposits form the transition between the organic
583 carbonates (Khodjaipak Fm.) and the overlying nodular gypsum. Similarly, UJS2 is overlain by sabkha
584 gypsum over the whole SW Gissar (**Fig. 12**), which reflects a progressive restriction and an increasing
585 salinity on the platform (Carmeille et al., 2018). In this scenario, the organic carbonates would form
586 contemporaneously of an evaporative, low energy carbonate lagoon rich in gypsum pseudomorphs (**Fig.**
587 **12**). This second hypothesis appears to be the most likely scenario, and will be used throughout the
588 paper.

589 **5.3. Sedimentological and geomicrobiological models for the Khodjaipak organic** 590 **carbonates**

591 **5.3.1. Depositional environment of the organic carbonates**

592 The fine-grained textures, conjugated with abundant and thin microbial laminations (**Figs 3 and 5**),
593 suggest a low-energy depositional environment for the Khodjaipak organic sediments (Droste, 1990;
594 Warren, 2011). The intercalation of thin shell beds (**Figs 3 and 4F**) indicates the punctual influence of
595 hydrodynamic events, probably storms, in this predominantly quiet environment. The presence of early
596 diagenetic sulfate pseudomorphs (**Fig. 5B**) may also indicate punctual hypersaline conditions within the
597 sediment (Warren, 2011). The Khodjaipak Fm. organic carbonates are overlain by **intertidal to shallow**
598 **subtidal** lagoon carbonates and then by supratidal sabkha chicken-wire gypsum (**Figs 1C and 3**). Similar
599 successions have been documented in the shallow subtidal to supratidal sequences of the Holocene Abu
600 Dhabi sabkha (e.g., Lokier and Steuber, 2008; Aref and Taj, 2018), but also in the Upper Jurassic to
601 Lowest Cretaceous Purbeck beds (northern France-southern UK; e.g., Shearman, 1966; West, 1975;
602 Schnyder et al., 2009) or in the Upper Permian of the Dolomites (Italy; e.g., Hardie, 1986). Jahnert and
603 Collins (2012) and Bouton et al. (2016) have also shown that thin storm shell beds can be trapped and
604 preserved within shallow water (< 1 m deep) hypersaline lagoon microbialites from Australia (Shark
605 Bay) and Cuba (Cayo Coco). In the absence of subaerial exposure evidence, we postulate that the
606 Khodjaipak Fm. was deposited in a shallow subtidal environment (**Fig. 13A**). This would imply that

607 **part of the pelagic fauna** (e.g., ammonites; **Figs 4 and 5**) could have undergone a post-mortem drift
608 (e.g., Olivero and Raffi, 2018). The documented benthic foraminifera (e.g., *Lenticulina* and
609 *Reinholdella*) are opportunistic, well adapted to low oxygen levels and can live in shallow water (Rita
610 et al., 2016). A shallow environment (depth of *ca.* 30 m) was hypothesized for the deposition of the
611 organic-rich part of the Middle-Upper Oxfordian Hanifa Fm. on the Arabian Platform (Warren, 2011).
612 Relatively shallow seas and the proximity of emerged lands or islands during the Khodjaipak Fm.
613 deposition are also consistent with the common occurrence of terrestrial-derived materials in
614 palynofacies, such as opaque and translucent phytoclasts, DSOM, WPWF, amorphized DBW, and
615 pollen and spores.

616 The highest TOC values are found in nodule-rich carbonate facies (F1b; **Fig. S1**). On the opposite,
617 quartz-rich siltstones have relatively low TOC, which indicates that carbonate production is associated
618 with OM concentration, while detrital influx probably favored OM dilution. Palynofacies yielding
619 opaque and translucent phytoclasts between 38 and 41 m (**Fig. 8**) indicate an increase of terrestrial
620 organic inputs at the top of the Khodjaipak Fm. (**Fig. 13A**). This interval rich in terrestrial phytoclasts
621 occurs after the decline in kaolinite proportion (**Fig. 3**) and precedes sabkha gypsum deposition. During
622 the Middle-Late Jurassic, periods marked by drastic changes in kaolinite are often interpreted as
623 variations in humidity conditions: high proportions in kaolinite point to humid conditions and low
624 kaolinite proportions to a drier climate (Pellenard and Deconinck, 2006; Schnyder et al., 2006; Brigaud
625 et al., 2014; Pellenard et al., 2014). Part of the opaque phytoclasts could also derive from wildfires in
626 the nearby continental areas. All these observations indicate that a climate aridification occurred during
627 the deposition of the Khodjaipak Fm. and could have culminated with the platform-wide development
628 of sabkha (Irgayli Fm.; **Figs 2, 12 and 13A**; Carmeille et al., 2018).

629 **5.3.2. Geomicrobiological model**

630 The thinly laminated microfabrics (**Fig. 5**), the presence of peloids and intra-carbonate OM (**Figs 5C**
631 **and 5E**), the potential preservation of EPS remnants (**Fig. 6C**) and the abundance of AOM in
632 palynofacies (**Fig. 8**), all suggest that most of the OM was produced by microorganisms (bacteria,
633 archaea and/or unicellular algae), notably in benthic microbial mats. The preservation of microbial

634 lamination can be partly explained by the scarcity of bioturbation, which in turns reflects the low
635 oxygenation of the bottom sediment (Warren, 2011). Trace elements concentrations and ratios indicate
636 alternating anoxic and suboxic conditions (**Fig. 11**). The potential development of contemporaneous
637 organic-poor carbonates in the SW Gissar (**Figs. 12 and 13A**) could indicate water stratification, where
638 the Khodjaipak Fm. accumulated in poorly oxygenated bottom water. These O₂-depleted conditions
639 promoted the preservation of OM -possibly through early sulfurization- and supported the development
640 of anaerobic microorganisms in the mats (e.g., methanogenic and methanotrophic microbes; **Fig. 13B**).
641 The two anoxic episodes are associated with the highest TOC, but also with the lowest $\delta^{13}\text{C}_{\text{carb}}$ and
642 $\delta^{15}\text{N}_{\text{tot}}$ (**Fig. 9**). During these episodes, we suggest that extensive denitrification decreased nitrate
643 availability and therefore, phytoplankton (including cyanobacteria) capable of using an alternate source
644 of nitrogen such as N₂ may have become quantitatively important, leading to a $\delta^{15}\text{N}_{\text{tot}}$ values close to
645 zero (**Fig. 9**; Quan and Falkowski, 2009). In addition, the dinitrogen gas increase could be a consequence
646 of the anammox bacterial activity, which converts ammonium from the anoxic water to N₂ by anaerobic
647 metabolic reaction (**Fig. 13B**; Kuypers et al., 2003; Kuenen, 2008).

648 In shallow hypersaline lagoons, the majority of OM derives from photosynthesis (Warren, 2011).
649 However, there is only indirect evidence for the presence of photoautotrophic microorganisms in the
650 Khodjaipak Fm. Sulfur-rich globules in OM-clay complexes (**Fig. 6D**) could indicate the activity of
651 anoxygenic phototrophs such as purple sulfur bacteria (Pace et al., 2018). Whether oxygenic
652 photosynthesis occurred in the Khodjaipak Fm. remains uncertain. The micritic and microsparitic
653 peloids observed in microbial boundstones (F1c; **Figs 5C and 6A to 6D**) are typically related to
654 microbial degradation of EPS. In modern mats, the degradation of some EPS components by
655 heterotrophic bacteria, e.g., sulfate-reducing bacteria (SRB), leads to the formation of carbonate peloids
656 by increasing alkalinity and releasing cations adsorbed by EPS such as calcium (e.g., Dupraz et al.,
657 2004; Visscher and Stolz, 2005; Pace et al., 2018). The presence of sulfate pseudomorphs in the
658 Khodjaipak Fm. (**Fig. 5B**) indicates that porewaters were sulfate-rich. Sulfates could have been reduced
659 by SRB to (hydrogen) sulfides (**Fig. 13B**) and part of the sulfides could have been subsequently
660 precipitated as pyrite or bound to part of the EPS through OM sulfurization. The study conducted by

661 Arp et al. (2008) in the Upper Jurassic of north Germany documents calcitized pseudomorphs of gypsum
662 with **very** low $\delta^{13}\text{C}_{\text{carb}}$ within stromatolites, suggesting oxygen-depleted sulfate-bearing environments
663 associated with high rates of methane production. These authors made the hypothesis that the gypsum
664 was replaced by magnesian calcite at the transition of suboxic and sulfidic zones within the mats **during**
665 **sulfate-driven anaerobic oxidation of methane (SD-AOM; Reeburgh, 2007; Himmler et al., 2018). The**
666 **$\delta^{13}\text{C}_{\text{carb}}$ values measured in the Khodjaipak Fm. (ranging from -10‰ to +2‰) are not negative enough**
667 **to support this process, but fit well with the $\delta^{13}\text{C}_{\text{carb}}$ range of hypersaline lake microbial mats with a high**
668 **organic productivity and SRB activity (Vasconcelos et al., 2006; Glunk et al., 2011; Dupraz et al., 2013).**
669 **Both geochemical and petrographic data suggest a strong contribution of microbial sulfate reduction to**
670 **carbonate precipitation. However, SD-AOM cannot be totally ruled out. Indeed, a late recrystallization**
671 **of carbonates in e.g., meteoric water, or a contribution of bioclast dissolution could have led to an**
672 **increase of the original $\delta^{13}\text{C}_{\text{carb}}$ values (e.g., De Boever et al., 2009).**

673 **5.3.3. Regional depositional model**

674 On epeiric platforms, OM accumulates in two types of mesohaline settings, often in association with
675 evaporites (Warren, 2011): (i) intrashelf basins or (ii) shelf edge depressions. Both cases imply a
676 tectonically and/or climatically-driven restriction of shelf water and the formation of a hydrographic
677 barrier partially isolating a **water body, leading to the formation of stratified brines**. In the Oxfordian
678 Hanifa Fm., reef or bioclastic platform rims built during transgressions, and subsequently isolated the
679 intrashelf basins during sea level falls (Carrigan et al., 1995; Warren, 2011). The Late Jurassic semi-
680 arid climate **also enhanced the** formation of anoxic/dysoxic saline brines in coastal lagoons and lakes
681 from the Purbeck Beds of Dorset (UK, Late Tithonian-Berriasian). Combined with freshwater inputs
682 linked to a climatic change toward slightly more humid conditions during the Berriasian, this ultimately
683 led to the development of water stratification and the deposition of OM-rich facies linked to enhanced
684 primary productivity in surface waters and its preservation in anoxic bottom water brines (Schnyder et
685 al., 2009). Similar examples of coastal marine sediment enriched in OM are known from Holocene
686 **coastal salinas and** hypersaline lagoons of Australia (Bauld, 1981; McKirdy et al., 1992; Coshell and
687 Rosen, 1994).

688 The Kugitang cliffs, located *ca.* 10 km south of Baglydara and 35 km east of Tubiegatan, display the
689 largest reefs outcropping in the SW Gissar (up to 80 m high; Ilyn and Fortunatova, 1988). These reefs
690 could be a stratigraphic equivalent of UJS1, where peri-reefal bioclastic deposits were documented (**Fig.**
691 **13A**; Carmeille et al., 2018). Such reefs complexes could have formed a hydrographic barrier limiting
692 water exchanges between the oxygenated inner platform water and the stratified brines in Tubiegatan.
693 Based on the correlation hypotheses **proposed Figure 12**, we built a four steps **carbonate shelf to anoxic**
694 **intrashelf lagoon** evolution scenario which shares some similarities -but is not strictly equivalent- with
695 that of the Purbeck Beds of Dorset or that of the above-mentioned Holocene Australian coastal lakes
696 and lagoons (**Fig. 13A**):

697 **-step 1:** the facies of the lower carbonate interval (sequences Tu1, Tu2 and the basis of Tu3) show
698 evidence for a good oxygenation of the water column. At that time, it is unknown whether Tubiegatan
699 was located on a seaward opened mid to outer shelf or within a well oxygenated, non-stratified lagoon.
700 At the top of the lower carbonate interval (Tu3 transgressive cycle, Luciaeformis SZ, Transversarium
701 Zone, Middle Oxfordian, **Fig. 3**), a flooding associated with a low sedimentation rate could explain the
702 formation of a subaqueous hardground. Reworking and erosion of coastal vegetalized areas due to the
703 transgression led to local inputs of wood debris, as indicated by opaque phytoclasts occurrences in the
704 palynofacies (**Fig. 8**). An intrashelf lagoon could have formed following the development of two
705 hydrographic barriers: (i) eastward, large coral reefs located to the south of the SW Gissar; (ii) a
706 hypothetical second hydrographic barrier located westward and/or southward (not outcropping).

707 **-step 2:** the presence of detrital kaolinite, usually formed during pedogenesis in intertropical climate,
708 suggests enhanced **water** precipitation at the beginning of the Khodjaipak Fm. deposition (Luciaeformis
709 to Schilli SZ, Transversarium Zone, Middle Oxfordian). Freshwater inputs, combined with limited
710 lagoon to basin water exchange leads to progressive water stratification. Extensive microbial mats
711 developed in the suboxic brines at the bottom of the intrashelf basin. Developing **benthic and possibly**
712 **planktonic** algal/bacterial productivity led to a relative increase in OM deposition ($\text{TOC} \leq 2\%$),
713 with palynofacies dominated by AOM. Shell beds may have derived from the **reworking** of peri-reefal
714 **sediments** by storm currents leading to possible punctual re-oxygenation of **the bottom** water mass.

715 -step 3: a regional aridification is attested by the disappearance of kaolinite and increase of IS-R1
716 possibly through illitization of original smectite, and characteristic of semi-arid climate and possible
717 wildfires as indicated by opaque wood fragments input. **The associated sea level drop** led to the exposure
718 of the reef complex and to an increasing isolation of the intrashelf basin, which became near permanently
719 anoxic (**Fig. 13A**; Schilli Subzone, Transversarium Zone, Middle Oxfordian). Step 3 is also the period
720 of maximum microbial mat development. The climatic conditions might still allow some periodic
721 freshwater inputs supporting primary productivity in surface waters and the local development of
722 ligneous aquatic or emerged coastal plants producing AOM and DBW, respectively (**Fig. 8**). The
723 shallow, restricted water may have promoted in situ amorphization/gelification processes of the DBW.
724 As a result of enhanced organic productivity (possibly from organic various sources) and developing
725 stratification, anoxia and OM deposition reached a maximum (TOC up to 6%).

726 -step 4: the increasing evaporation progressively decreasing water depth and lowering freshwater input,
727 could have limited water stratification. The resulting mixing of surface and bottom water led to the
728 oxygenation of the bottom of the intrashelf basin **and to OM oxidation** (TOC \leq 1%; **Fig. 8**). Intertidal
729 to shallow subtidal lagoon deposits, **including stromatolites**, prograded and progressively filled the
730 accommodation space (Schilli to post-Schilli Subzones, Middle Oxfordian). **Finally the nodular gypsum**
731 **accumulation records the development** of a large scale sabkha covering the whole SW Gissar region
732 (**Fig. 3**). These sabkha deposits are either anterior to- or partly contemporaneous with the thick salt-
733 anhydrite series of the Gaurdak Fm. (Kirshin, 2007; Abdullaev et al., 2010; Carmeille et al., 2018). At
734 this time, regional subsidence is very low (Brunet et al., 2017). Compression and uplifts in the Afghan
735 and Central Iranian blocks related to the closure of the Waras-Panjaw Ocean (Central Afghanistan)
736 probably leads to the restriction of the ADB and to the deposition of the Gaurdak salt (Barrier et al.,
737 2018). Overall, the organic-rich deposits of Khodjaipak Fm. may record the onset of the isolation of the
738 ADB from more open areas (e.g., the South Caspian Basin). In this case the new datings provided by
739 ammonites identification at Tubiegatan would demonstrate that this disconnection would have begun at
740 the end of the Middle Oxfordian. This tectonic disconnection, combined with a regional aridification

741 could have led to the progressive increase of evaporation and subsequent organic-rich deposits in
742 intrashelf depressions on the carbonate platform.

743 **5.4. Context and origin of worldwide-scale organic-rich accumulations during the** 744 **Oxfordian-Kimmeridgian**

745 The Early Oxfordian-Early Kimmeridgian period is characterized by the multiplication of organic-rich
746 deposits worldwide and could be considered as a Late Jurassic Ocean Anoxic Event as proposed by
747 Trabucho-Alexandre et al. (2012) and Martinez & Dera (2015). Major source rocks developed during
748 this period, e.g., the Hanifa Fm., the Kimmeridge Clay Fm., the Smackover Fm. (Warren, 2011). **Figure**
749 **14** compiles the facies and composition of these organic-rich formations. On the Arabian Platform, the
750 Lower to Upper Oxfordian organic-rich Hanifa Fm. accumulated in small and semi-isolated intrashelf
751 basins, where seawater was stratified and OM accumulated in dysoxic to anoxic bottom water (Droste,
752 1990; Carrigan et al., 1995; Vahrenkamp et al., 2015). The progressive isolation of these basins could
753 be the consequence of an uplift of the Eastern margin of the Arabian Plate. The restriction of the
754 intrashelf basins subsequently led to the evolution from normal marine shallow-water carbonates during
755 the Kimmeridgian (Jubaila Fm.) to restricted-marine and evaporitic deposits during the Tithonian (Arab
756 A, B, C and Hith Fms). In Wadi Nisah (Saudi Arabia), the Hanifa Fm. is composed of fine-grained
757 carbonates and biosiliceous facies (Hawtah Member) overlain by organic-rich silty carbonates
758 alternating with burrowed skeletal facies (Ulayyah Member; Eltom et al., 2017). These deposits are
759 interpreted to reflect the circulation of nutrient-rich currents derived from shelf edge upwellings into the
760 intrashelf basins (Eltom et al., 2017). The basal sequence C of the Smackover Fm. and its distal
761 equivalent, the Haynesville Shales, are major source rocks in the United States Gulf Coast. These
762 formations include organic-rich (up to 6% TOC) and biosiliceous lime mudstones, which accumulated
763 in anoxic intrashelf basins delimited by carbonate platforms and islands (Heydari et al., 1997; Hammes
764 et al., 2011; **Fig. 14**). Some of these facies could be of microbial origin (Hammes et al., 2011). In the
765 Neuquen Basin (Argentina), the unit 1 of La Manga Fm. consists of basinal organic rich shale-limestone
766 **sequences** (up to 4.5% TOC), which are locally rich in radiolarians (Palma et al., 2014). These deposits
767 could have accumulated in half grabens, close to the hanging wall of normal faults, while shallow water

768 carbonates could have been produced on the foot wall. They are overlain by Middle-Upper Oxfordian
769 intertidal stromatolites with fenestrae and mud-cracks (Palma et al., 2015; **Fig. 14**) and finally by sabkha
770 deposits of the Auquilco Fm., recording an overall shallowing trend. A common stratigraphic pattern
771 characterizes these Middle to Upper Oxfordian organic-rich formations: (i) subtidal normal marine
772 carbonates are overlain by (ii) mesohaline organic facies (often microbial). This succession reflects the
773 progressive stratification of the water, sometimes associated with- or followed by an increase of the
774 salinity. Then, (iii) intertidal to shallow subtidal carbonates are overlain by (iv) sabkha deposits,
775 indicating the filling of the accommodation space and a further increase of salinity. The quasi-
776 contemporaneous formation of intrashelf basins on the northern and southern margins of the Tethys, in
777 the Gulf of Mexico and on the eastern margin of the Pacific during the Middle to Late Oxfordian could
778 reflect the early stages of the large-scale compressive tectonic events known as Late Cimmerian or Neo
779 Cimmerian in western central Asia (Late Jurassic to Early Cretaceous; i.e. Boulin, 1990) leading to
780 margin inversions.

781 The influence of these multiple organic accumulations on the global carbon cycle can be questioned. In
782 the subalpine basin, a short-term negative $\delta^{13}\text{C}_{\text{carb}}$ excursion (*ca.* 0.5-2‰) in the Transversarium Zone
783 punctuates a long-term positive trend encompassing the Plicatilis–Transversarium interval (Padden et
784 al., 2001; Louis-Schmid et al., 2007; Rais et al., 2007). A negative excursion was also measured in
785 nodular micritic limestones known as Knollenkalk in the Swiss Jura Mountains (Rais et al., 2007; **Fig.**
786 **14**). These excursions could be the result of gas hydrate dissociation (Jenkyns, 2003). The compilation
787 of western Tethyan belemnite $\delta^{13}\text{C}$ by Martinez and Dera (2015) shows a major negative carbon isotope
788 excursion (amplitude of *ca.* 4‰) at the Middle to Late Oxfordian transition (Transversarium–Bifurcatus
789 Zone; **Fig. 14**). This period coincides with a maximum in the high eccentricity of the 9 Myr orbital cycle
790 as defined by Martinez & Dera (2015). According to these authors the maxima of eccentricity leading
791 to altered climatic conditions. Stratification of the water and anoxia develop preferentially during
792 seasonal humid phases, inducing terrestrial runoff and nutrient inputs. During arid phases, increasing
793 evaporation leads to homogenization of the water mass (Martinez and Dera, 2015). The
794 sedimentological, geochemical and mineralogical evolution of the Khodjaipak Fm. (**Fig. 13A-B**) fits

795 well with this scenario. In addition, the CO₂ outgassing from protracted magmatic activity along
796 spreading ridges and subduction zones could have induced warming climate during the Late Jurassic,
797 leading to increase the flux of nutrients and, as a consequence, the biological productivity (e.g., Jones
798 and Jenkyns, 2001; Georgiev et al., 2017). However, no lines of evidence of this long-lived volcanic
799 activity were still published. Overall, the multiplication of OM storage events during the top of the
800 Middle Oxfordian and the base of the Upper Oxfordian (**Fig. 14**) could have resulted from the
801 conjunction of (i) an orbital-driven, changing seasonal climate coupled to (ii) an increase in continental
802 and/or oceanic nutrient inputs and (iii) the initiation of tectonic inversion on several margins.

803 **CONCLUSION**

804 The Khodjaipak Fm. is composed of organic-rich carbonates, marls and siltstones which were deposited
805 on a vast part of the Amu Darya Basin. These deposits were newly dated to the Middle Oxfordian,
806 Transversarium Zone (Luciaeformis and Schilli Subzones). The predominant facies are organic
807 laminated siltstones, nodular mudstones reaching ~6% of total organic carbon, and thinly laminated
808 microbial boundstones. These organic-rich deposits are overlain by shallow water lagoon and sabkha
809 deposits. Palynofacies and petrographic analyses show that a significant proportion of the OM was
810 produced in benthic microbial mats together with possible secondary contributions of algal/bacterial
811 primary production in surface waters and local developments of aquatic macrophytes. Rock-Eval
812 pyrolysis analyses indicate that the OM is mature (reaching the oil window), and that a minimal burial
813 depth of 2-3 km was reached. The concentrations and ratios of trace metallic element record two anoxic
814 episodes punctuated by dysoxic periods. These anoxic episodes are associated with the highest total
815 organic carbon values, enhanced aquatic primary production (possibly from several sources as indicated
816 by palynofacies), $\delta^{15}\text{N}_{\text{tot}}$ close to zero and the most negative $\delta^{13}\text{C}_{\text{carb}}$ values. Both microfabrics and
817 palynofacies indicate a significant contribution of microbial **communities** to the formation of carbonates.
818 The presence of sulfate pseudomorphs, sulfur globules and pyrite could indicate bacterial sulfur cycling.
819 The light $\delta^{13}\text{C}_{\text{carb}}$ signature of stromatolites and carbonate nodules could be related to precipitation
820 influenced by **sulfate reduction**. Overall, the Khodjaipak Fm. is interpreted to have formed in a shallow
821 water stratified, probably slightly hypersaline (intrashelf?) basin, periodically isolated from the

822 contemporaneous lagoon by pre-existing carbonate platform reliefs (e.g., coral reefs). The Middle-
823 **Upper** Oxfordian is characterized by the multiplication of comparable organic-rich deposits in the
824 northern and southern Tethys, in the Central Atlantic and in the Pacific. Some of these deposits could
825 also have formed in shallow water anoxic conditions, which contrasts with the basin anoxia model
826 characterizing **some** Cretaceous OAE. Anoxic conditions **may** have been enhanced by the conjunction
827 of a contrasted arid/humid climate and the tectonic inversion of several margins. The multiplication of
828 such shallow water anoxic episodes could have led to major carbon cycle perturbations from the Middle
829 Oxfordian till the Early Kimmeridgian.

830

831 ACKNOWLEDGEMENTS

832 This study was funded by Total S.A. The scientists of the Institute of Geology and Geophysics of Uzbek
833 Academy of Sciences of Tashkent (Uzbekistan), especially Irina Sidorova and Dmitriy Mordvintsev,
834 are acknowledged for their logistic support in the field. The authors express their gratitude to Grégoire
835 Bex for its assistance in the field, Léa Pigot and Philippe Blanc for the preparation of the thin sections,
836 and Anne-Lise Santoni, Théophile Coquerez and Ludovic Bruneau for their assistance with analyses.

837

838

839

Bibliography

- 840
841
842 Abdullaev, G.S., 2004. Biostratigraphy, lithofacies and oil and gas perspectives of the Amu-Darya
843 northern margin Jurassic carbonates. Abstract of the thesis, Geology and Geophysics Institute,
844 archives, Tashkent, 39 p. (in Russian).
- 845 Abdullaev, G.S., 1999. Detailing of Stratigraphy of Upper Jurassic Carbonate Complex of Western
846 Uzbekistan - Basis for Increasing Effectiveness of Oil-Gas Exploration 33, 297–304.
- 847 Abdullaev, G.S., Mirkamalov, H.H., 2001. Stratigraphy of the Jurassic high-gamma activity rocks of
848 the Bukhara-Khiva region and its importance for the modelisation of the carbonate formation.
849 Collect. Tr. IGIRNIGM Tashkent 13–24.
- 850 Abdullaev, G.S., Mirkamalov, H.H., Evseeva, G.B., 2010. Oil and gas bearing reefal facies of the
851 Jurassic carbonate unit of the Amu-Darya basin (southern and southwestern Uzbekistan) and
852 their correlation with reef creation within the paleobasins of the Tethys. Theor. Pract. Asp. Oil
853 Gas Geol. Cent. Asia Solut. Mod. Probl. Domain NGGI Tashkent 39–49.
- 854 Aref, M.A., Taj, R.J., 2018. Recent evaporite deposition associated with microbial mats, Al-Kharrar
855 supratidal–intertidal sabkha, Rabigh area, Red Sea coastal plain of Saudi Arabia. *Facies* 64,
856 28. <https://doi.org/10.1007/s10347-018-0539-y>
- 857 Arp, G., Ostertag-Henning, C., Yücekent, S., Reitner, J., Thiel, V., 2008. Methane-related microbial
858 gypsum calcitization in stromatolites of a marine evaporative setting (Münder Formation,
859 Upper Jurassic, Hils Syncline, north Germany). *Sedimentology* 55, 1227–1251.
860 <https://doi.org/10.1111/j.1365-3091.2007.00944.x>
- 861 Barrier, E., Vrielynck, B., Brouillet, J.-F., Brunet, M.-F., 2018. Paleotectonic Reconstruction of the
862 Central Tethyan Realm. Tectono-Sedimentary-Palinspastic maps from Late Permian to
863 Pliocene. CCGM/CGMW, Paris, <http://www.ccgm.org>. Atlas of 20 maps (scale: 1/15 000
864 000).
- 865 Bartolini, A., Baumgartner, P.O., Guex, J., 1999. Middle and Late Jurassic radiolarian palaeoecology
866 versus carbon-isotope stratigraphy. *Palaeogeogr. Palaeoclimatol. Palaeoecol.* 145, 43–60.
867 [https://doi.org/10.1016/S0031-0182\(98\)00097-2](https://doi.org/10.1016/S0031-0182(98)00097-2)
- 868 Baudin, F., Tribouvillard, N., Laggoun-Défarge, F., Lichtfouse, E., Monod, O., Gardin, S., 1999.
869 Depositional environment of a Kimmeridgian carbonate ‘black band’ (Akkuyu Formation,
870 south-western Turkey). *Sedimentology* 46, 589–602. <https://doi.org/10.1046/j.1365-3091.1999.00226.x>
- 871 Baudin, F., Tribouvillard, N., Trichet, J., 2007. Géologie de la matière organique. EDP sciences.
- 872 Bauld, J., 1981. Geobiological role of cyanobacterial mats in sedimentary environments: production
873 and preservation of organic matter. *BMR J. Aust. Geol. Geophys.* 6, 307–317.
- 874 Behar, F., Beaumont, V., Penteado, H.L.D.B., 2001. Rock-Eval 6 Technology: Performances and
875 Developments. *Oil Gas Sci. Technol.* 56, 111–134. <https://doi.org/10.2516/ogst:2001013>
- 876 Bernier, P., Enay, R., 1972. Figures d’émersion temporaire et indices de sédimentation a très faible
877 profondeur dans le Portlandien et le Kimméridgien supérieur (Calcaires en plaquettes) du
878 Grand-Colombier-de-Culoz (Ain, France). *Bull. Société Géologique Fr.* S7-XIV, 281–292.
879 <https://doi.org/10.2113/gssgfbull.S7-XIV.1-5.281>
- 880 Besnosov, N.V., Mitta, V.V., 1995. Upper Jurassic Ammonitids and Black Shales of Central Asia. -
881 Russ. Geol. Oil Inst. VNIGNI.
- 882 Boulin, J., 1990. Neocimmerian events in Central and Western Afghanistan. *Tectonophysics* 175,
883 285–315. [https://doi.org/10.1016/0040-1951\(90\)90177-A](https://doi.org/10.1016/0040-1951(90)90177-A)
- 884 Bouton, A., Vennin, E., Pace, A., Bourillot, R., Dupraz, C., Thomazo, C., Brayard, A., Désaubliaux,
885 G., Visscher, P.T., 2016. External controls on the distribution, fabrics and mineralization of
886 modern microbial mats in a coastal hypersaline lagoon, Cayo Coco (Cuba). *Sedimentology* 63,
887 972–1016. <https://doi.org/10.1111/sed.12246>
- 888 Brigaud, B., Vincent, B., Carpentier, C., Robin, C., Guillocheau, F., Yven, B., Huret, E., 2014. Growth
889 and demise of the Jurassic carbonate platform in the intracratonic Paris Basin (France):
890 Interplay of climate change, eustasy and tectonics. *Mar. Pet. Geol.* 27, 853–894
- 891 Brumsack, H.-J., 2006. The trace metal content of recent organic carbon-rich sediments: Implications
892 for Cretaceous black shale formation. *Palaeogeogr. Palaeoclimatol. Palaeoecol.* 232, 344–361.
893 <https://doi.org/10.1016/j.palaeo.2005.05.011>
894

- 895 Brunet, M.-F., Ershov, A.V., Korotaev, M.V., Melikhov, V.N., Barrier, E., Mordvintsev, D.O.,
896 Sidorova, I.P., 2017. Late Palaeozoic and Mesozoic evolution of the Amu Darya Basin
897 (Turkmenistan, Uzbekistan). *Geol. Soc. Lond. Spec. Publ.* 427, 89–144.
898 <https://doi.org/10.1144/SP427.18>
- 899 Carignan, J., Hild, P., Désaubliaux, G., Morel, J., Yeghicheyan, D., 2001. Routine Analyses of Trace
900 Elements in Geological Samples using Flow Injection and Low Pressure On-Line Liquid
901 Chromatography Coupled to ICP-MS: A Study of Geochemical Reference Materials BR, DR-
902 N, UB-N, AN-G and GH. *Geostand. Newsl.* 25, 187–198. <https://doi.org/10.1111/j.1751-908X.2001.tb00595.x>
- 904 Cariou, E., Hantzpergue, P., 1997. Groupe Français d'Etudes du Jurassique, Biostratigraphie du
905 Jurassique Ouest-Européen et Méditerranéen. Zonations parallèles et distribution des
906 invertébrés et microfossiles. *Bulletin des Centres de Recherches et Exploration Production*
907 d'Elf-Aquitaine, v. 17, p. 400.
- 908 Carneille, M., Bourillot, R., Brunet, M.-F., Pellenard, P., Fürsich, F.T., Schnyder, J., Barrier, E.,
909 Blanpied, C., Sidorova, I., 2018. Architecture and sedimentary evolution of the southwestern
910 Gissar carbonate platform (Uzbekistan) during the Middle–Late Jurassic. *Mar. Pet. Geol.* 97,
911 437–465. <https://doi.org/10.1016/j.marpetgeo.2018.07.021>
- 912 **Carpentier, C., Lathuilière, B., Ferry, S., Sausse, J., 2007. Sequence stratigraphy and**
913 **tectonosedimentary history of the Upper Jurassic of the Eastern Paris Basin (Lower and**
914 **Middle Oxfordian, northeastern France). *Sedimentary Geology*, 197(3-4), 235-266.**
- 915 Carrigan, W.J., Cole, G.A., Colling, E.L., Jones, P.J., 1995. Geochemistry of the Upper Jurassic
916 Tuwaiq Mountain and Hanifa Formation Petroleum Source Rocks of Eastern Saudi Arabia, in:
917 Katz, B.J. (Ed.), *Petroleum Source Rocks, Casebooks in Earth Sciences*. Springer Berlin
918 Heidelberg, Berlin, Heidelberg, pp. 67–87. https://doi.org/10.1007/978-3-642-78911-3_5
- 919 Catuneanu, O., Galloway, W.E., Kendall, C.G.S.C., Miall, A.D., Posamentier, H.W., Strasser, A.,
920 Tucker, M.E., 2011. Sequence Stratigraphy: Methodology and Nomenclature. *Newsl. Stratigr.*
921 44, 173–245. <https://doi.org/10.1127/0078-0421/2011/0011>
- 922 Chamley, H., 1989. Clay Formation Through Weathering, in: *Clay Sedimentology*. Springer, Berlin,
923 Heidelberg, pp. 21–50. https://doi.org/10.1007/978-3-642-85916-8_2
- 924 Collin, P.Y., Kershaw, S., Tribouvillard, N., Forel, M.B., Crasquin, S., 2015. Geochemistry of post-
925 extinction microbialites as a powerful tool to assess the oxygenation of shallow marine water
926 in the immediate aftermath of the end-Permian mass extinction. *Int. J. Earth Sci.* 104, 1025–
927 1037. <https://doi.org/10.1007/s00531-014-1125-3>
- 928 Coshell, L., Rosen, M.R., 1994. Stratigraphy and Holocene History of Lake Hayward, Swan Coastal
929 Plain Wetlands, western Australia. In: Renaut R. and Last W. (eds), *Sedimentology and*
930 *Geochemistry of Modern and Ancient Saline Lakes*. SEPM, Tulsa, Sp. Publ. 50, 173–188.
- 931 **De Boever, E., Birgel, D., Thiel, V., Muechez, P., Peckmann, J., Dimitrov, L., & Swennen, R., 2009.**
932 **The formation of giant tubular concretions triggered by anaerobic oxidation of methane as**
933 **revealed by archaeal molecular fossils (Lower Eocene, Varna, Bulgaria). *Palaeogeography,***
934 ***Palaeoclimatology, Palaeoecology*, 280(1-2), 23-36.**
935 <https://doi.org/10.1016/j.palaeo.2009.05.010>
- 936 Dellisanti, F., Pini, G.A., Baudin, F., 2010. Use of Tmax as a thermal maturity indicator in orogenic
937 successions and comparison with clay mineral evolution. *Clay Miner.* 45, 115–130.
938 <https://doi.org/10.1180/claymin.2010.045.1.115>
- 939 Dera, G., Brigaud, B., Monna, F., Laffont, R., Pucéat, E., Deconinck, J.-F., Pellenard, P., Joachimski,
940 M.M., Durlet, C., 2011. Climatic ups and downs in a disturbed Jurassic world. *Geology* 39,
941 215–218. <https://doi.org/10.1130/G31579.1>
- 942 Droste, H., 1990. Depositional cycles and source rock development in an epeiric intra-platform basin:
943 the Hanifa Formation of the Arabian peninsula. *Sediment. Geol., Processes and Patterns in*
944 *Epeiric Basins* 69, 281–296. [https://doi.org/10.1016/0037-0738\(90\)90054-W](https://doi.org/10.1016/0037-0738(90)90054-W)
- 945 Dupraz, C., Visscher, P.T., Baumgartner, L.K., Reid, R.P., 2004. Microbe–mineral
946 interactions: early carbonate precipitation in a hypersaline lake (Eleuthera Island, Bahamas).
947 *Sedimentology* 51, 745–765. <https://doi.org/10.1111/j.1365-3091.2004.00649.x>

- 948 Dupraz, C., Fowler, A., Tobias, C., Visscher, P.T., 2013. Stromatolitic knobs in Storr's Lake (San
949 Salvador, Bahamas): a model system for formation and alteration of laminae. *Geobiology* 11,
950 527–548. <https://doi.org/10.1111/gbi.12063>
- 951 Eltom, H.A., Rankey, E.C., Hasiotis, S.T., Gonzalez, L.A., Cantrell, D.A., 2017. Impact of Upwelling
952 On Heterozoan, Biosiliceous, and Organic-rich Deposits: Jurassic (Oxfordian) Hanifa
953 Formation, Saudi Arabia. *J. Sediment. Res.* 87, 1235–1258.
954 <https://doi.org/10.2110/jsr.2017.71>
- 955 Enay, R., Le Nindre, Y.-M., Mangold, C., Manivit, J., Vaslet, D., 1987. Le Jurassique d'Arabie
956 saoudite centrale. In: R. Enay (Ed.), *Le Jurassique d'Arabie Saoudite Centrale*. Geobios, Lyon,
957 Mémoire Spécial, no. 9, p. 13–65.
- 958 Espitalié, J., Deroo, G., Marquis, F., 1985. La pyrolyse Rock-Eval et ses applications. Première partie.
959 *Rev. Inst. Fr. Pétrole* 40, 563–579. <https://doi.org/10.2516/ogst:1985035>
- 960 Georgiev, S.V., Stein, H.J., Hannah, J.L., Xu, G., Bingen, B., Weiss, H.M., 2017. Timing, duration,
961 and causes for Late Jurassic–Early Cretaceous anoxia in the Barents Sea. *Earth Planet. Sci.*
962 *Lett.* 461, 151–162. <https://doi.org/10.1016/j.epsl.2016.12.035>
- 963 **Glunk, C., Dupraz, C., Braissant, O., Gallagher, K. L., Verrecchia, E. P., Visscher, P. T., 2011.**
964 **Microbially mediated carbonate precipitation in a hypersaline lake, Big Pond (Eleuthera,**
965 **Bahamas). *Sedimentology*, 58(3), 720–736. <https://doi.org/10.1111/j.1365-3091.2010.01180.x>**
- 966 Hammes, U., Hamlin, H.S., Ewing, T.E., 2011. Geologic analysis of the Upper Jurassic Haynesville
967 Shale in east Texas and west Louisiana. *AAPG Bull.* 95, 1643–1666.
968 <https://doi.org/10.1306/02141110128>
- 969 **Hardenbol, J. A. N., Thierry, J., Farley, M. B., Jacquin, T., De Graciansky, P. C., & Vail, P. R., 1998.**
970 **Mesozoic and Cenozoic sequence chronostratigraphic framework of European basins.**
- 971 Hardie, L.A., 1986. Ancient carbonate tidal-flat deposits. *Colo. Sch. Mines Q.* 81, 37–57.
- 972 Heydari, E., Wade, W.J., Anderson, L.C., 1997. Depositional Environments, Organic Carbon
973 Accumulation, and Solar-Forcing Cyclicity in Smackover Formation Lime Mudstones,
974 Northern Gulf Coast. *AAPG Bull.* 81, 760–774.
- 975 Himmler, T., Smrzka, D., Zwicker, J., Kasten, S., Shapiro, R.S., Bohrmann, G., Peckmann, J., 2018.
976 Stromatolites below the photic zone in the northern Arabian Sea formed by calcifying
977 chemotrophic microbial mats. *Geology*. <https://doi.org/10.1130/G39890.1>
- 978 Ilyn, V.D., Fortunatova, N.K., 1988. Methods of Prediction and Exploration in Oil and Gas Bearing
979 Reefal Complexes. *Nedra* 201, 200.
- 980 Immenhauser, A., Kenter, J.A.M., Ganssen, G., Bahamonde, J.R., Vliet, A.V., Saher, M.H., 2002.
981 Origin and Significance of Isotope Shifts in Pennsylvanian Carbonates (Asturias, NW Spain).
982 *J. Sediment. Res.* 72, 82–94. <https://doi.org/10.1306/051701720082>
- 983 Jadoul F., Berra F., Garzanti E., 1998. The Tethys Himalayan passive margin from Late Triassic to
984 Early Cretaceous (South Tibet). *J. Asian Earth Sci.* 16:173–194.
- 985 Jahnert, R.J., and Collins, L.B., 2012. Characteristics, distribution and morphogenesis of subtidal
986 microbial systems in Shark Bay, Australia. *Marine Geology*, v. 303–306, p. 115–136.
- 987 Jain, K.P., Garg, R., Kumar, S., Singh, I.B., 1984. Upper Jurassic dinoflagellate biostratigraphy of
988 Spiti Shale (Formation), Malla Johar area, Tethys Himalaya, India. *J. Palaeontol. Soc. India*
989 29, 67–83.
- 990 Jenkyns, H.C., 2003. Evidence for rapid climate change in the Mesozoic–Palaeogene greenhouse
991 world. *Philos. Trans. R. Soc. Lond. Math. Phys. Eng. Sci.* 361, 1885–1916.
992 <https://doi.org/10.1098/rsta.2003.1240>
- 993 Jones, C.E., Jenkyns, H.C., 2001. Seawater Strontium Isotopes, Oceanic Anoxic Events, and Seafloor
994 Hydrothermal Activity in the Jurassic and Cretaceous. *Am. J. Sci.* 301, 112–149.
995 <https://doi.org/10.2475/ajs.301.2.112>
- 996 Kirshin, A.V., 2007. Complex geological-geophysical researches of the Gissar block. *Oil Gas Inst.*
997 Tashkent.
- 998 Klett, T.R., Schenk, C.J., Wandrey, C.J., Charpentier, R.R., Brownfield, M.E., Pitman, J.K., Pollastro,
999 R.M., Cook, T.A., Tennyson, M.E., 2012. Assessment of undiscovered oil and gas resources
1000 of the Amu Darya Basin and Afghan-Tajik Basin Provinces, Afghanistan, Iran, Tajikistan,
1001 Turkmenistan, and Uzbekistan, 2011 (USGS Numbered Series No. 2011–3154), Fact Sheet.
1002 U.S. Geological Survey, Reston, VA.

- 1003 Klett, T.R., Wandrey, C.J., Ulmishek, G.F., Amirzada, A., 2006. Afghan resource assessment fed
1004 positive outlook for exploration. *Oil Gas J.* 104.
- 1005 **Kuenen, J. G., 2008. Anammox bacteria: from discovery to application. *Nature Reviews*
1006 *Microbiology*, 6(4), 320.**
- 1007 Kuypers, M.M.M., Sliemers, A.O., Lavik, G., Schmid, M., Jørgensen, B.B., Kuenen, J.G., Damsté,
1008 J.S.S., Strous, M., Jetten, M.S.M., 2003. Anaerobic ammonium oxidation by anammox
1009 bacteria in the Black Sea. *Nature*, 422, 608–611.
- 1010 Lézin, C., Andreu, B., Pellenard, P., Bouchez, J.-L., Emmanuel, L., Fauré, P., Landrein, P., 2013.
1011 Geochemical disturbance and paleoenvironmental changes during the Early Toarcian in NW
1012 Europe. *Chem. Geol.* 341, 1–15. <https://doi.org/10.1016/j.chemgeo.2013.01.003>
- 1013 Lokier, S., Steuber, T., 2008. Quantification of Carbonate-Ramp Sedimentation and Progradation
1014 Rates for the Late Holocene Abu Dhabi Shoreline. *J. Sediment. Res.* 78, 423–431.
1015 <https://doi.org/10.2110/jsr.2008.049>
- 1016 Lokier, S.W., Andrade, L.L., Court, W.M., Dutton, K.E., Head, I.M., Land, C. van der, Paul, A.,
1017 Sherry, A., 2017. A new model for the formation of microbial polygons in a coastal sabkha
1018 setting. *Depositional Rec.* 3, 201–208. <https://doi.org/10.1002/dep2.33>
- 1019 Louis-Schmid, B., Rais, P., Bernasconi, S.M., Pellenard, P., Collin, P.-Y., Weissert, H., 2007. Detailed
1020 record of the mid-Oxfordian (Late Jurassic) positive carbon-isotope excursion in two
1021 hemipelagic sections (France and Switzerland): A plate tectonic trigger? *Palaeogeogr.*
1022 *Palaeoclimatol. Palaeoecol.* 248, 459–472. <https://doi.org/10.1016/j.palaeo.2007.01.001>
- 1023 Marshall, J.D., 1992. Climatic and oceanographic isotopic signals from the carbonate rock record and
1024 their preservation. *Geol. Mag.* 129, 143–160. <https://doi.org/10.1017/S0016756800008244>
- 1025 Martinez, M., Dera, G., 2015. Orbital pacing of carbon fluxes by a ~9-My eccentricity cycle during
1026 the Mesozoic. *Proc. Natl. Acad. Sci.* 112, 12604–12609.
1027 <https://doi.org/10.1073/pnas.1419946112>
- 1028 McArthur, A.D., Kneller, B.C., Souza, P.A., Kuchle, J., 2016. Characterization of deep-marine
1029 channel-levee complex architecture with palynofacies: An outcrop example from the Rosario
1030 Formation, Baja California, Mexico. *Mar. Pet. Geol.* 73, 157–173.
1031 <https://doi.org/10.1016/j.marpetgeo.2016.02.030>
- 1032 McKirdy, D.M., Padley, D., MacDonald, F., Warren, J., Hayball, A., Von Der Borch, C., 1992.
1033 Coorong lacustrine carbonates as analogues of ancient evaporite-associated hydrocarbon
1034 source rocks, in: AAPG International Conference and Exhibition, Sydney, Abstracts. pp. 63–
1035 64.
- 1036 McLennan, S.M., 2001. Relationships between the trace element composition of sedimentary rocks
1037 and upper continental crust. *Geochem. Geophys. Geosystems* 2.
1038 <https://doi.org/10.1029/2000GC000109>
- 1039 Meer, D.G.V.D., Zeebe, R.E., Hinsbergen, D.J.J. van, Sluijs, A., Spakman, W., Torsvik, T.H., 2014.
1040 Plate tectonic controls on atmospheric CO₂ levels since the Triassic. *Proc. Natl. Acad. Sci.*
1041 201315657. <https://doi.org/10.1073/pnas.1315657111>
- 1042 Mirkamalov, H.H., Abdullaev, G.S., Evseeva, G.B., Sudareva, E.U., Ahmedova, M.R., Haneeva, F.R.,
1043 Muratova, L.M., 2005. The studying of the Jurassic sediments of the Beshkent trough and
1044 nearby areas to precise its lithological-facial and stratigraphic structure and to determine its
1045 relations with the pre-Mesozoic complexes. Report, Oil and Gas Institute, Tashkent (in
1046 Russian). 111.
- 1047 Mitta, V.V., 1992. Callovian Pachyceratids (Ammonoidea) Of Central Asia. *Paleontol. J.* 26, 4.
- 1048 Mitta, V.V., Besnosov, N.V., 2007. Jurassic System Cephalopods. *Palaeontol. Atlas Phaneroz. Faunas*
1049 *Floras Uzb. Volume II Mesoz. Cenozoic Jurass. Cretac. Palaeogene*, Republic of Uzbekistan
1050 State Committee on Geology and Mineral Resources, Tashkent, Uzbekistan.
- 1051 Moore, D.M., Reynolds, R.C., 1989. X-ray Diffraction and the Identification and Analysis of Clay
1052 Minerals. Oxford university press New York.
- 1053 Mordvintsev, D., 2015. Tectono-stratigraphic evolution of the northern margin of the Amu-Darya
1054 basin in Uzbekistan (Bukhara-Khiva and Southwestern Gissar regions). PhD thesis. University
1055 P. & M. Curie, Paris, France.

- 1056 Mukhopadhyay, P. K., Wade, J. A., & Kruge, M. A., 1997. Source Rocks for Condensate and Gas-
 1057 Examples from Jurassic-Cretaceous Sediments of Scotian Basin, Nova Scotia, Eastern
 1058 Canada.
- 1059 Nugmanov, A.H., 2010. Laws of formation of traps and oil and gas fields, oil and gas potential of the
 1060 northern side of the Amu-Darya syncline. Geology Geophysics Institute, Tashkent,
 1061 Uzbekistan.
- 1062 O'Dogherty, L., Aguado, R., Baumgartner, P.O., Bill, M., Goričan, Š., Sandoval, J., Sequeiros, L.,
 1063 2018. Carbon-isotope stratigraphy and pelagic biofacies of the Middle–Upper Jurassic
 1064 transition in the Tethys–Central Atlantic connection. *Palaeogeogr. Palaeoclimatol. Palaeoecol.*
 1065 507, 129–144. <https://doi.org/10.1016/j.palaeo.2018.07.006>
- 1066 Oehler, J.H., 1984. Carbonate Source Rocks in the Jurassic Smackover Trend of Mississippi,
 1067 Alabama, and Florida 30, 63–69.
- 1068 Olivero, E.B., Raffi, M.E., 2018. Onshore–offshore trends in Campanian ammonite facies from the
 1069 Marambio Group, Antarctica: Implications for ammonite habitats. *Cretac. Res., Cretaceous*
 1070 *ammonites: a volume in memory of Richard A. Reymont (1926–2016)* 88, 79–89.
 1071 <https://doi.org/10.1016/j.cretres.2017.03.001>
- 1072 Pace, A., Bourillot, R., Bouton, A., Vennin, E., Braissant, O., Dupraz, C., Duteil, T., Bundeleva, I.,
 1073 Patrier, P., Galaup, S., Yokoyama, Y., Franceschi, M., Virgone, A., Visscher, P.T., 2018.
 1074 Formation of stromatolite lamina at the interface of oxygenic–anoxygenic photosynthesis.
 1075 *Geobiology* 16, 378–398. <https://doi.org/10.1111/gbi.12281>
- 1076 Padden, M., Weissert, H., Rafelis, M. de, 2001. Evidence for Late Jurassic release of methane from
 1077 gas hydrate. *Geology* 29, 223–226. [https://doi.org/10.1130/0091-](https://doi.org/10.1130/0091-7613(2001)029<0223:EFLJRO>2.0.CO;2)
 1078 [7613\(2001\)029<0223:EFLJRO>2.0.CO;2](https://doi.org/10.1130/0091-7613(2001)029<0223:EFLJRO>2.0.CO;2)
- 1079 Palma, R., Bressan, G.S., Kietzmann, D.A., Riccardi, A.C., Martín-Chivelet, J., López-Gómez, J.,
 1080 2014. Palaeoenvironmental significance of middle Oxfordian deep marine deposits from La
 1081 Manga Formation, Neuquén Basin, Argentina. *J. Iber. Geol.* 40, 507–520.
 1082 https://doi.org/10.5209/rev_JIGE.2014.v40.n3.43804
- 1083 Palma, R., Kietzmann, D.A., Comerio, M., Martín-Chivelet, J., López-Gómez, J., Bressan, G.S., 2015.
 1084 Oxfordian microbial laminites from La Manga Formation, Neuquén Basin, Argentina:
 1085 Remarkable nanobacteria preservation.
- 1086 Pearce, C.R., Hesselbo, S.P., Coe, A.L., 2005. The mid-Oxfordian (Late Jurassic) positive carbon-
 1087 isotope excursion recognised from fossil wood in the British Isles. *Palaeogeogr.*
 1088 *Palaeoclimatol. Palaeoecol.* 221, 343–357. <https://doi.org/10.1016/j.palaeo.2005.03.004>
- 1089 Pellenard, P., Deconinck, J.-F., 2006. Mineralogical variability of Callovo-Oxfordian clays from the
 1090 Paris Basin and the Subalpine Basin. *Comptes Rendus Geosci., Le Callovo-Oxfordien du*
 1091 *bassin de Paris : du contexte géologique à la modélisation de ses propriétés* 338, 854–866.
 1092 <https://doi.org/10.1016/j.crte.2006.05.008>
- 1093 Pellenard, P., Tramoy, R., Pucéat, E., Huret, E., Martinez, M., Bruneau, L., Thierry, J., 2014. Carbon
 1094 cycle and sea-water palaeotemperature evolution at the Middle–Late Jurassic transition,
 1095 eastern Paris Basin (France). *Mar. Pet. Geol., Present and past transfers in a sedimentary*
 1096 *aquifer – aquitard system: a 2000 meter deep drill-hole in the Mesozoic of the Paris Basin* 53,
 1097 30–43. <https://doi.org/10.1016/j.marpetgeo.2013.07.002>
- 1098 Petschick, R., 2001. ‘MacDiff 4.2.5 manual.’ (Johann Wolfgang Goethe-Universität Frankfurt am
 1099 Main: Frankfurt)
- 1100 Quan, T.M., Falkowski, P.G., 2009. Redox control of N:P ratios in aquatic ecosystems. *Geobiology* 7,
 1101 124–139. doi:10.1111/j.1472-4669.2008.00182.x
- 1102 Rais, P., Louis-Schmid, B., Bernasconi, S.M., Weissert, H., 2007. Palaeoceanographic and
 1103 palaeoclimatic reorganization around the Middle–Late Jurassic transition. *Palaeogeogr.*
 1104 *Palaeoclimatol. Palaeoecol.* 251, 527–546. <https://doi.org/10.1016/j.palaeo.2007.05.008>
- 1105 **Raven, M. R., Fike, D. A., Gomes, M. L., Webb, S. M., 2019. Chemical and isotopic evidence for**
 1106 **organic matter sulfurization in redox gradients around mangrove roots. *Frontiers in Earth***
 1107 ***Science*, 7, 98. <https://doi.org/10.3389/feart.2019.00098>**
- 1108 Reeburgh, W.S., 2007. Oceanic Methane Biogeochemistry. *Chem. Rev.* 107, 486–513.
 1109 <https://doi.org/10.1021/cr050362v>

- 1110 Rickard, D., Mussmann, M., Steadman, J.A., 2017. Sedimentary Sulfides. *Elements* 13, 117–122.
 1111 <https://doi.org/10.2113/gselements.13.2.117>
- 1112 Rita, P., Reolid, M., Duarte, L.V., 2016. Benthic foraminiferal assemblages record major
 1113 environmental perturbations during the Late Pliensbachian–Early Toarcian interval in the
 1114 Peniche GSSP, Portugal. *Palaeogeogr. Palaeoclimatol. Palaeoecol.* 454, 267–281.
 1115 <https://doi.org/10.1016/j.palaeo.2016.04.039>
- 1116 Schnyder, J., Ruffell, A., Deconinck, J.-F., Baudin, F., 2006. Conjunctive use of spectral gamma-ray
 1117 logs and clay mineralogy in defining late Jurassic–early Cretaceous palaeoclimate change
 1118 (Dorset, U.K.). *Palaeogeogr. Palaeoclimatol. Palaeoecol.* 229, 303–320.
 1119 <https://doi.org/10.1016/j.palaeo.2005.06.027>
- 1120 Schnyder, J., Baudin, F., Deconinck, J.-F., 2009. Occurrence of organic-matter-rich beds in Early
 1121 Cretaceous coastal evaporitic setting (Dorset, UK): a link to long-term palaeoclimate changes?
 1122 *Cretac. Res.* 30, 356–366. <https://doi.org/10.1016/j.cretres.2008.07.014>
- 1123 Schnyder, J., Stetten, E., Baudin, F., Pruski, A.M., Martinez, P., 2017. Palynofacies reveal fresh
 1124 terrestrial organic matter inputs in the terminal lobes of the Congo deep-sea fan. *Deep Sea*
 1125 *Res. Part II Top. Stud. Oceanogr., Organic carbon transfer and ecosystem functioning in the*
 1126 *terminal lobes of the Congo deep-sea fan: The Conglobe multidisciplinary study* 142, 91–108.
 1127 <https://doi.org/10.1016/j.dsr2.2017.05.008>
- 1128 Sharland, P., Archer, R., Casey, D.M., Davies, R.B., Hall, S.H., Heward, A.P., Horbury, A.D.,
 1129 Simmons, M. 2001. *Arabian Plate Sequence Stratigraphy*. *GeoArabia Special Publication*, 2
 1130 372p.
- 1131 **Shawar, L., Halevy, I., Said-Ahmad, W., Feinstein, S., Boyko, V., Kamyshny, A., Amrani, A., 2018.**
 1132 **Dynamics of pyrite formation and organic matter sulfurization in organic-rich carbonate**
 1133 **sediments. *Geochimica et Cosmochimica Acta*, 241, 219-239.**
 1134 <https://doi.org/10.1016/j.gca.2018.08.048>
- 1135 Shearman, D.J., 1966. Origin of marine evaporites by diagenesis. *Trans Inst Min Met.* 75, 208–215.
- 1136 Storme, J.-Y., Dupuis, C., Schnyder, J., Quesnel, F., Garel, S., Iakovleva, A.I., Iacumin, P., Di Matteo,
 1137 A., Sebilio, M., Yans, J., 2012. Cycles of humid-dry climate conditions around the P/E
 1138 boundary: new stable isotope data from terrestrial organic matter in Vasterival section (NW
 1139 France). *Terra Nova* 24, 114–122. <https://doi.org/10.1111/j.1365-3121.2011.01044.x>
- 1140 Sucha, V., Kraus, I., Gerthofferova, H., Petes, J., Serekova, M., 1993. Smectite to illite conversion in
 1141 bentonites and shales of the East Slovak Basin. *Clay Miner.* 28, 243–243.
 1142 <https://doi.org/10.1180/claymin.1993.028.2.06>
- 1143 Trabucho-Alexandre, J., Dirkx, R., Veld, H., Klaver, G., & de Boer, P. L., 2012. Toarcian
 1144 black shales in the Dutch Central Graben: record of energetic, variable depositional conditions
 1145 during an oceanic anoxic event. *Journal of sedimentary Research*, 82(2), 104-120.
 1146 <https://doi.org/10.2110/jsr.2012.5>
- 1147 Tribovillard, N., Desprairies, A., Lallier-Vergès, E., Bertrand, P., Moureau, N., Ramdani, A.,
 1148 Ramanampisoa, L., 1994. Geochemical study of organic-matter rich cycles from the
 1149 Kimmeridge Clay Formation of Yorkshire (UK): productivity versus anoxia. *Palaeogeogr.*
 1150 *Palaeoclimatol. Palaeoecol.* 108, 165–181. [https://doi.org/10.1016/0031-0182\(94\)90028-0](https://doi.org/10.1016/0031-0182(94)90028-0)
- 1151 Tribovillard, N., Trentesaux, A., Trichet, J., Défarge, C., 2000. A Jurassic counterpart for modern
 1152 kopara of the Pacific atolls: lagoonal, organic matter-rich, laminated carbonate of Orbagnoux
 1153 (Jura Mountains, France). *Palaeogeogr. Palaeoclimatol. Palaeoecol.* 156, 277–288.
 1154 [https://doi.org/10.1016/S0031-0182\(99\)00145-5](https://doi.org/10.1016/S0031-0182(99)00145-5)
- 1155 **Tribovillard, N., Riboulleau, A., Lyons, T., Baudin, F., 2004. Enhanced trapping of molybdenum by**
 1156 **sulfurized marine organic matter of marine origin in Mesozoic limestones and shales.**
 1157 ***Chemical Geology*, 213(4), 385-401. <https://doi.org/10.1016/j.chemgeo.2004.08.011>**
- 1158 Tribovillard, N., Algeo, T.J., Lyons, T., Riboulleau, A., 2006. Trace metals as paleoredox and
 1159 paleoproductivity proxies: An update. *Chem. Geol.* 232, 12–32.
 1160 <https://doi.org/10.1016/j.chemgeo.2006.02.012>
- 1161 Tyson, R.V., 1995. Abundance of Organic Matter in Sediments: TOC, Hydrodynamic Equivalence,
 1162 Dilution and Flux Effects, in: *Sedimentary Organic Matter*. Springer, Dordrecht, pp. 81–118.
 1163 https://doi.org/10.1007/978-94-011-0739-6_5

- 1164 Tyson, R.V., 2012. Sedimentary organic matter: organic facies and palynofacies. Springer
1165 Science & Business Media.
- 1166 Ulmishek, G.F., 2004. Petroleum geology and resources of the Amu-Darya basin, Turkmenistan,
1167 Uzbekistan, Afghanistan, and Iran (USGS Numbered Series No. 2201- H), Bulletin.
- 1168 Vahrenkamp, V.C., Van Laer, P., Franco, B., Celentano, M.A., Grelaud, C., Razin, P., 2015. Late
1169 Jurassic to Cretaceous Source Rock Prone Intra-Shelf Basins of the Eastern Arabian Plate–
1170 Interplay between Tectonism, Global Anoxic Events and Carbonate Platform Dynamics, in:
1171 International Petroleum Technology Conference.
- 1172 Vasconcelos, C., Warthmann, R., McKenzie, J. A., Visscher, P. T., Bittermann, A. G., van Lith, Y.
1173 2006. Lithifying microbial mats in Lagoa Vermelha, Brazil: modern Precambrian relics?.
1174 *Sedimentary Geology*, 185(3-4), 175-183. <https://doi.org/10.1016/j.sedgeo.2005.12.022>
- 1175 Visscher, P.T., Stolz, J.F., 2005. Microbial mats as bioreactors: populations, processes, and products,
1176 in: Noffke, N. (Ed.), *Geobiology: Objectives, Concepts, Perspectives*. Elsevier, Amsterdam,
1177 pp. 87–100. <https://doi.org/10.1016/B978-0-444-52019-7.50009-7>
- 1178 Warren, J.K., 2011. Evaporitic source rocks: mesohaline responses to cycles of “famine or feast” in
1179 layered brines. *Int Assoc Sediment Spec Publ* 43, 315–392.
- 1180 West, I.M., 1975. Evaporites and associated sediments of the basal Purbeck Formation (Upper
1181 Jurassic) of Dorset. *Proc. Geol. Assoc.* 86, 205–225. [https://doi.org/10.1016/S0016-](https://doi.org/10.1016/S0016-7878(75)80101-5)
1182 [7878\(75\)80101-5](https://doi.org/10.1016/S0016-7878(75)80101-5)
- 1183 Whitaker, M.F., Giles, M.R., Cannon, S.J.C., 1992. Palynological review of the Brent Group, UK
1184 sector, north sea. *Geol. Soc. Lond. Spec. Publ.* 61, 169–202.
1185 <https://doi.org/10.1144/GSL.SP.1992.061.01.10>
- 1186 Wilson, J.L., 1975. *Carbonate Facies in Geologic History*. Springer.
1187

1188

FIGURE LEGENDS

1189 **Fig. 1: A)** Location of the Amu Darya and Afghan-Tajik basins in western Central Asia. ADF, Amu
1190 Darya Fault; C Ust F, Central Ustyurt Fault; STS F, South Tien Shan Fault; UKFFZ, Uchbash-Karshi
1191 Flexure Fault Zone; Za F, Zaravshan Fault. **B)** Location of the Tubiegatan section in the SW Gissar
1192 Range and geological setting of the study area (Surkhandarya province). Gau, Gaurdak section. **C-D)**
1193 View of the Khodjaipak Fm. in the Tubiegatan section (C) and of the Tubiegatan anticline (D).

1194

1195 **Fig. 2:** Simplified stratigraphic chart of the Middle–Upper Jurassic formations in the NE part of the
1196 Amu Darya Basin based on the works carried out by Fürsich et al., 2017, Carmeille et al., 2018 and this
1197 study.

1198

1199 **Fig. 3:** Sedimentological section of the Kugitang carbonates and the Khodjaipak Formation in the
1200 Tubiegatan area. The vertical variations of bulk mineralogy, clay-mineral assemblages and Total
1201 Organic Carbon (TOC) are plotted along the section. High frequency transgressive-regressive cycles
1202 and ammonite biostratigraphy are indicated to the left side. For the location of the section, refer to Fig.
1203 1B.

1204

1205 **Fig. 4:** Sedimentary facies of the Tubiegatan section: **A)** Ammonite imprint at the surface of a
1206 bioturbated horizon, lower carbonate interval; **B-C)** Examples of *Thalassinoides* burrows (Bur.) in the
1207 limestones, lower carbonate interval (F2b); **D)** Black to brownish marls to siltstones (F1a), Khodjaipak
1208 Fm; **E)** Black nodule of organic-rich mud-carbonate, intercalated in brown marls to siltstones (F1b),
1209 Khodjaipak Fm; **F)** Shell (storm?) bed (F1d) composed of disarticulated bivalves and brachiopod
1210 fragments, Khodjaipak Fm.

1211

1212 **Fig. 5:** Laminated organic microbial boundstone (F1c), Khodjaipak Fm.: **A-B)** Alternation of
1213 millimetric and infra-millimetric carbonate and organic lamina. Note the occurrence of sulfate
1214 pseudomorphs in B (yellow arrows). **C)** Laminae composed of organic-rich carbonate peloids (orange
1215 arrow). **D)** Planktonic foraminifera trapped in a stromatolite lamina. **E)** Detail of an organic-carbonate
1216 mineral couplet. Organic matter is concentrated in the organic-rich laminae, but also between the
1217 microspar crystals of the carbonate laminae. **F)** Yellow to brown aggregates (yellow arrow), which could
1218 be hydrocarbon droplets. A is a field photograph, B is a scanned thin section and C to F are polarizing
1219 microscope images (plane polarized light).

1220

1221 **Fig. 6:** SEM images and EDS elemental mapping in the organic microbial boundstone (F1c). **A-B)**
1222 Micritic to microsparitic peloids in an alveolar organic network (A) and EDS element mapping (B). On
1223 the EDS map, calcite peloids are green (Ca-rich), the alveolar organic matrix (probable EPS remnants)
1224 is pink (C-rich), while clays are grey (Al-rich). **C)** Close-up view of Fig. 6A. **D)** Organic matter-clay
1225 aggregate. Small bright sulfur rich globules (SG) are also locally observed. **E-F)** SEM picture (E) and
1226 EDS map (F) of a peloidal lamina. Calcite peloids (green) are surrounded by a mix of quartz (Si-rich;
1227 blue), clay (grey) and iron oxides (red).

1228

1229 **Fig. 7:** Hydrogen index (HI) versus T_{max} diagram. Circle diameter is proportional to TOC, and their
1230 color is related to the palynofacies intervals defined on Figure 8.

1231

1232 **Fig. 8:** Vertical evolution of palynofacies. DBW, degraded brown wood; AOM, amorphous organic
1233 matter; DSOM, dark structureless organic matter; WFPF, well-preserved wood fragments. **A to D)**
1234 Palynofacies photomicrographs. **A-B)** Orange to dark amorphous organic matter (AOM), sample 09-
1235 E3, 37.2 m. **C)** Dark AOM with rectangular shape, sample 09-E2, 37 m. **D)** Translucent phytoclasts,
1236 sample 13-E4, 21 m.

1237

1238 **Fig. 9:** Vertical evolution of organic ($\delta^{13}\text{C}_{\text{org}}$), inorganic ($\delta^{13}\text{C}_{\text{carb}}$ and $\delta^{18}\text{O}_{\text{carb}}$) and total ($\delta^{15}\text{N}_{\text{tot}}$) isotope
1239 ratio along the Tubiegatan section.

1240

1241 **Fig. 10:** $\delta^{13}\text{C}_{\text{carb}}-\delta^{18}\text{O}_{\text{carb}}$ cross-plots for the Tubiegatan section: Khodjaipak Fm., lower and upper
1242 carbonate intervals. The range of values for the south west Gissar platform carbonates (Callovian
1243 Sequence in green; Upper Jurassic Sequence in pink) are indicated.

1244

1245 **Fig. 11:** Vertical evolution of TOC, Mo_{xs} and some trace metal elemental ratios: U/Th and V/Cr along
1246 the Khodjaipak Fm. Within grey intervals (AI1 and AI2), the ratios point to anoxic conditions.

1247

1248 **Fig. 12:** Two correlation hypotheses between the Tubiegatan section and the south-west Gissar platform,
1249 based on the $\delta^{13}\text{C}_{\text{carb}}$ and the sequence stratigraphy.

1250

1251 **Fig. 13:** **(A)** Depositional scenario and **(B)** geomicrobiological model for the Khodjaipak Fm. in the
1252 Tubiegatan area, and relationship with the SW Gissar carbonate platform.

1253

1254 **Fig. 14:** Age, composition and distribution of the OM-rich sedimentary formation during the Oxfordian-
1255 Early Kimmeridgian period. The second-order NW Tethyan T/R cycles are from Hardenbol et al, 1998.
1256 The smoothed $\delta^{13}\text{C}_{\text{carb}}$ curve is from Martinez and Dera, 2015.

1257

1258 **Fig. S1:** **A)** Plot of CaCO_3 vs. TOC values for the Tubiegatan samples. Note that the highest values are
1259 associated to carbonate samples. **B-C)** Kaolinite vs. TOC: **(B)** percentage of kaolinite relative to bulk
1260 rock and **(C)** percentage of kaolinite relative to the clay fraction. **D)** R1-type illite-smectite mixed-layer
1261 (IS-R1) vs. TOC. The percentage of IS-R1 is relative to the clay fraction.

1262

1263

1264 **Fig. S2:** Van Krevelen diagram: Hydrogen index (HI) vs. oxygen index (OI).

1265

1266

1267 **Fig. S3:** Vertical evolution of the C/N ratio.

1268

1269

1270

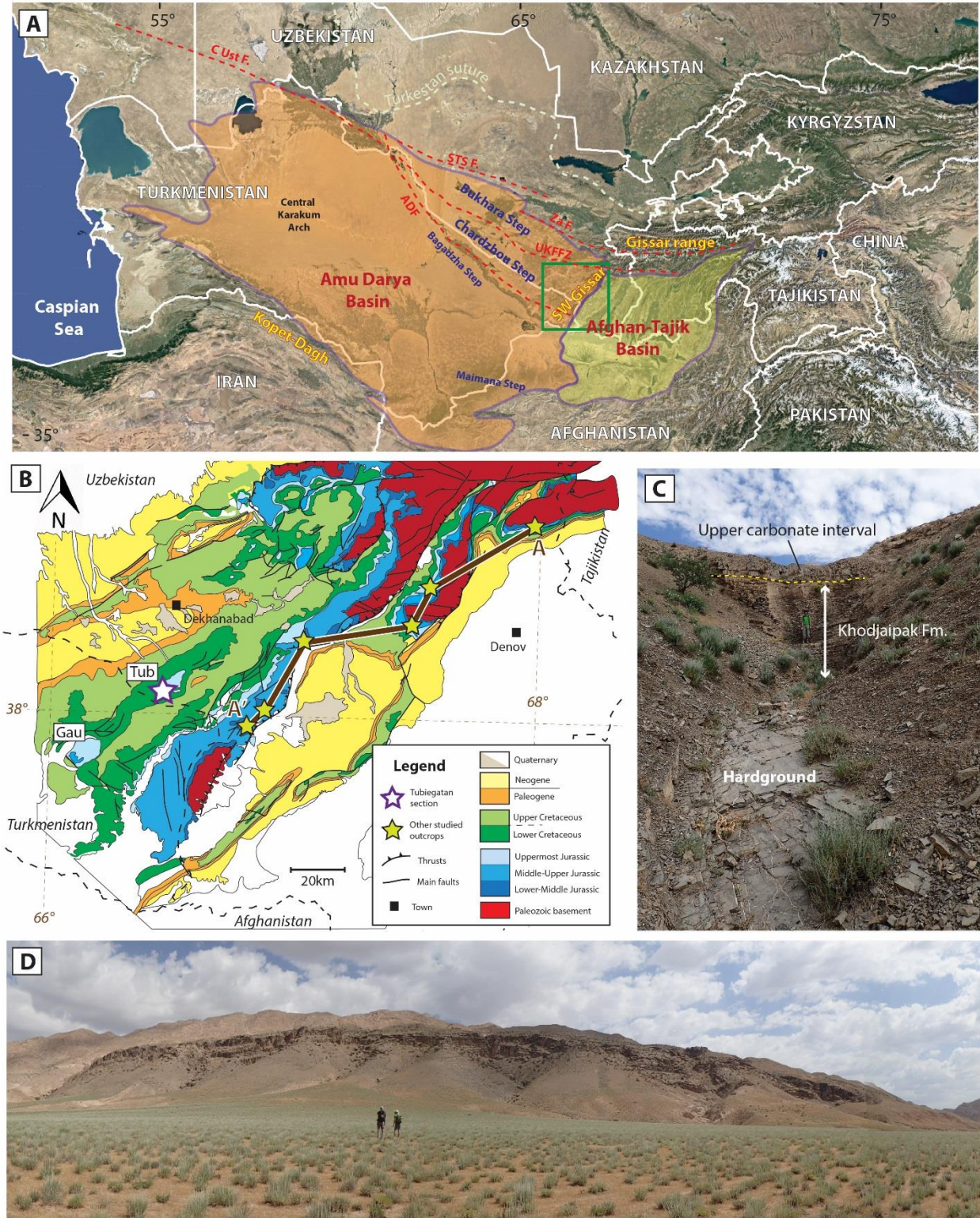


Fig. 1: A) Location of the Amu Darya and Afghan-Tajik basins in western Central Asia. ADF, Amu Darya Fault; C Ust F, Central Ustyurt Fault; STS F, South Tien Shan Fault; UKFFZ, Uchbash-Karshi Flexure Fault Zone; Za F, Zaravshan Fault. **B)** Location of the Tubiegatan section in the SW Gissar Range and geological setting of the study area (Surkhandarya province). Gau, Gaurdak section. **C-D)** View of the Khodjaipak Fm. in the Tubiegatan section (C) and of the Tubiegatan anticline (D).

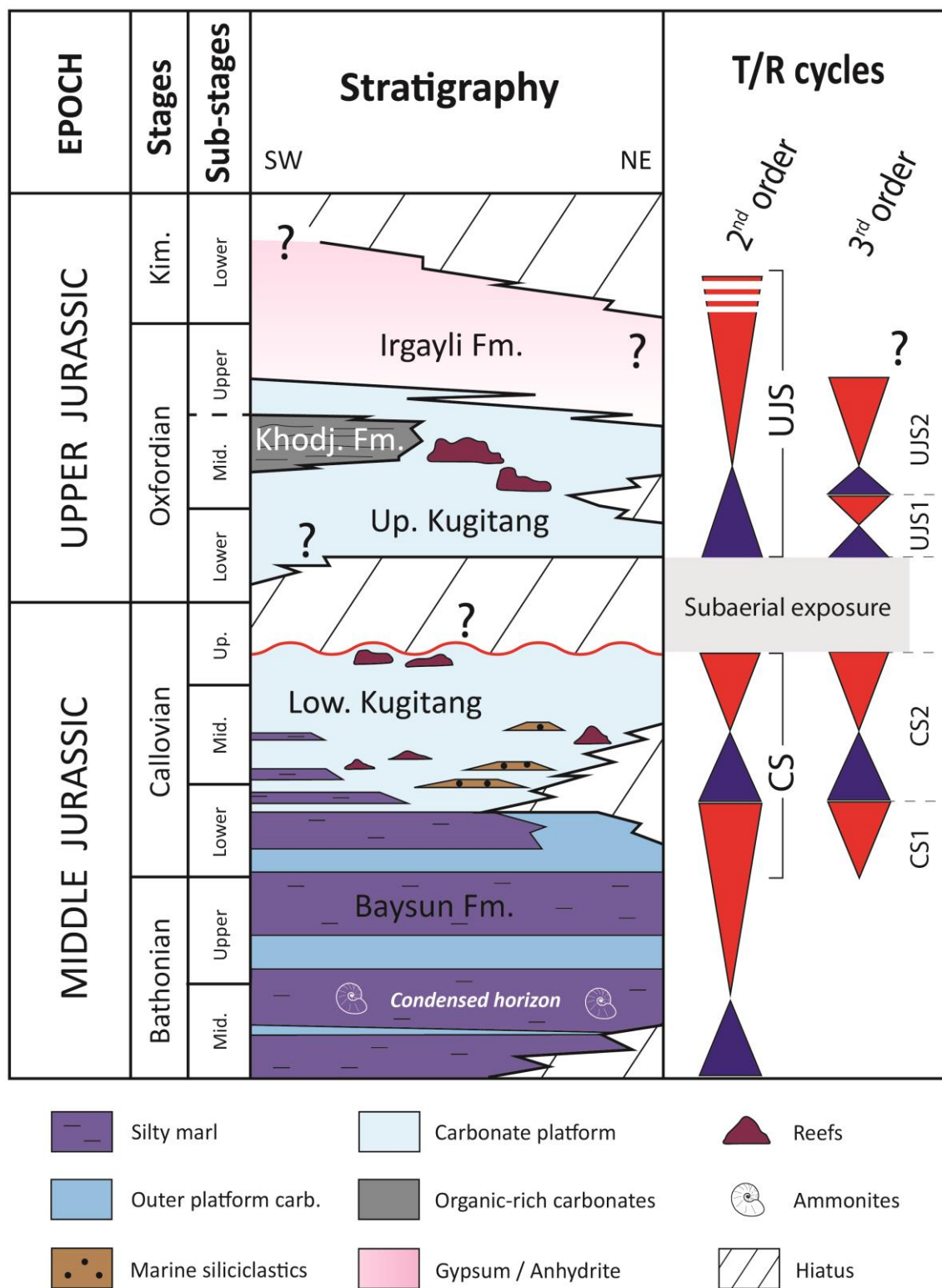


Fig. 2: Simplified stratigraphic chart of the Middle–Upper Jurassic formations in the NE part of the Amu Darya Basin based on the works carried out by Fürsich et al., 2017, Carmeille et al., 2018 and this study.

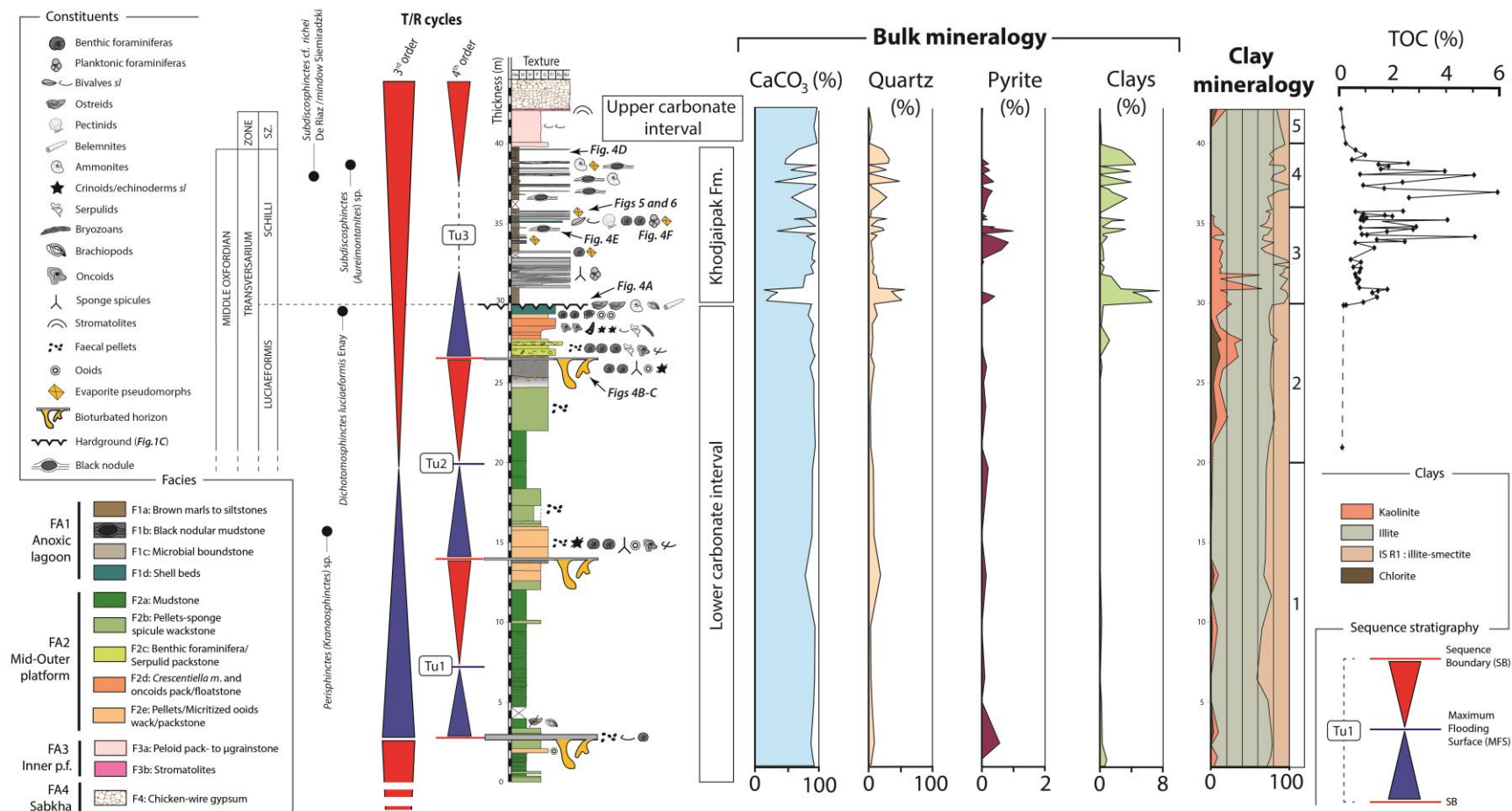


Fig. 3: Sedimentological section of the Kugitang carbonates and the Khodjaiapak Formation in the Tubiegatan area. The vertical variations of bulk mineralogy, clay-mineral assemblages and Total Organic Carbon (TOC) are plotted along the section. High frequency transgressive-regressive cycles and ammonite biostratigraphy are indicated to the left side. For the location of the section, refer to Fig. 1B.

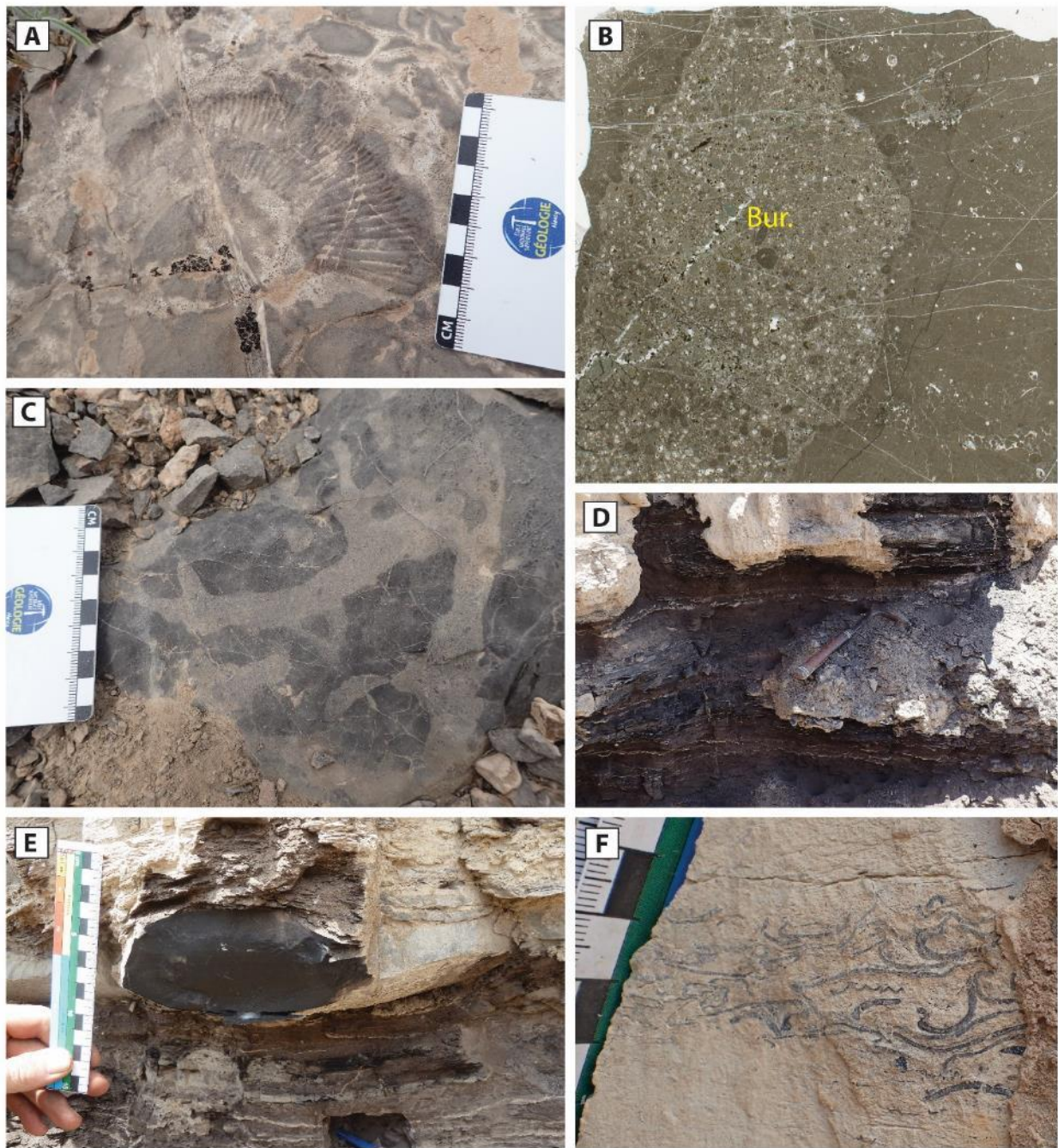


Fig. 4: Sedimentary facies of the Tubiegatan section: **A)** Ammonite imprint at the surface of a bioturbated horizon, lower carbonate interval; **B-C)** Examples of *Thalassinoides* burrows (Bur.) in the limestones, lower carbonate interval (F2b); **D)** Black to brownish marls to siltstones (F1a), Khodjaipak Fm; **E)** Black nodule of organic-rich mud-carbonate, intercalated in brown marls to siltstones (F1b), Khodjaipak Fm; **F)** Shell (storm?) bed (F1d) composed of disarticulated bivalves and brachiopod fragments, Khodjaipak Fm.

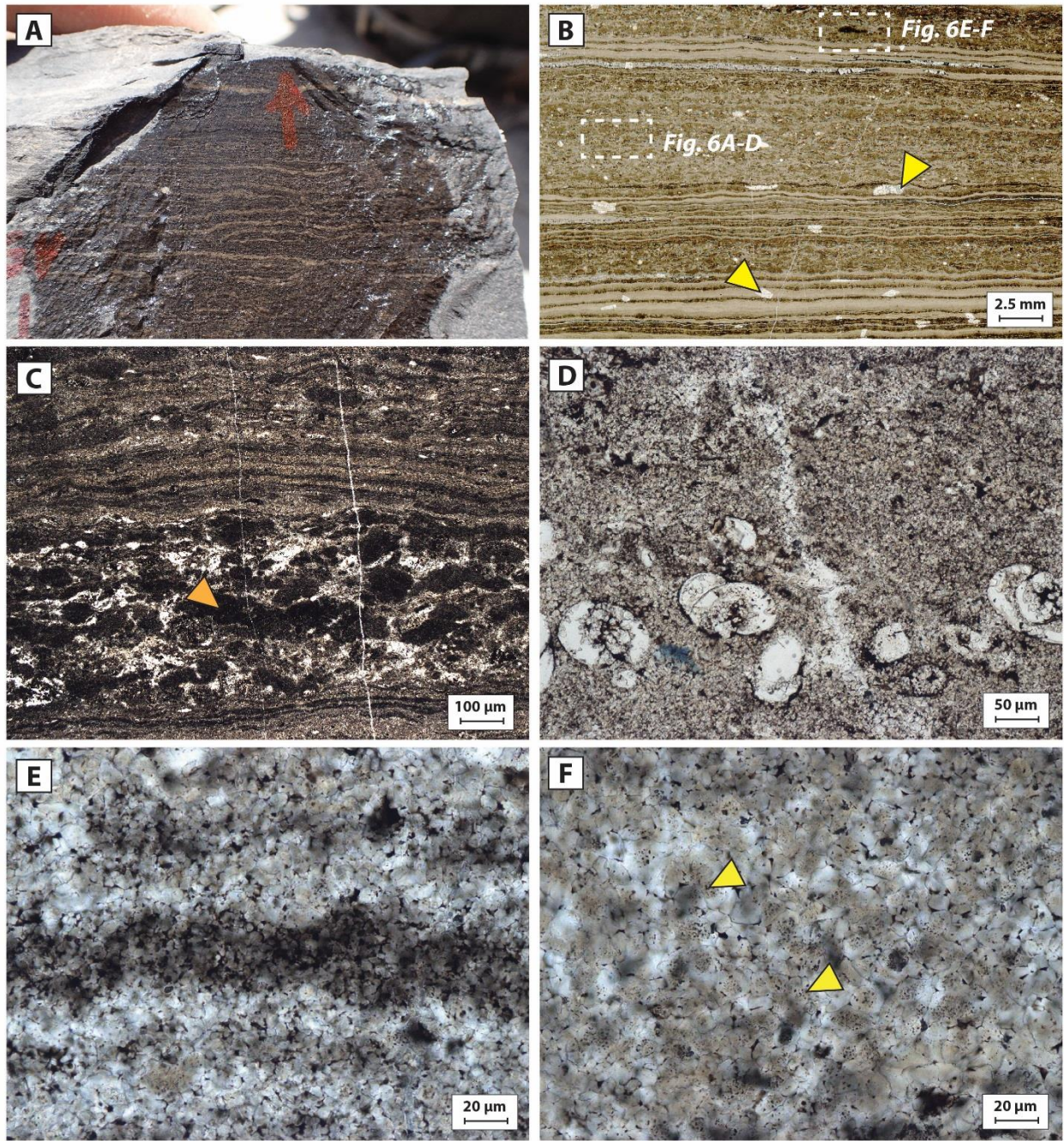


Fig. 5: Laminated organic microbial boundstone (F1c), Khodjaipak Fm.: **A-B)** Alternation of millimetric and infra-millimetric carbonate and organic lamina. Note the occurrence of sulfate pseudomorphs in B (yellow arrows). **C)** Laminae composed of organic-rich carbonate peloids (orange arrow). **D)** Planktonic foraminifera trapped in a stromatolite lamina. **E)** Detail of an organic-carbonate mineral couplet. Organic matter is concentrated in the organic-rich laminae, but also between the microspar crystals of the carbonate laminae. **F)** Yellow to brown aggregates (yellow arrow), which could be hydrocarbon droplets. A is a field photograph, B is a scanned thin section and C to F are polarizing microscope images (plane polarized light).

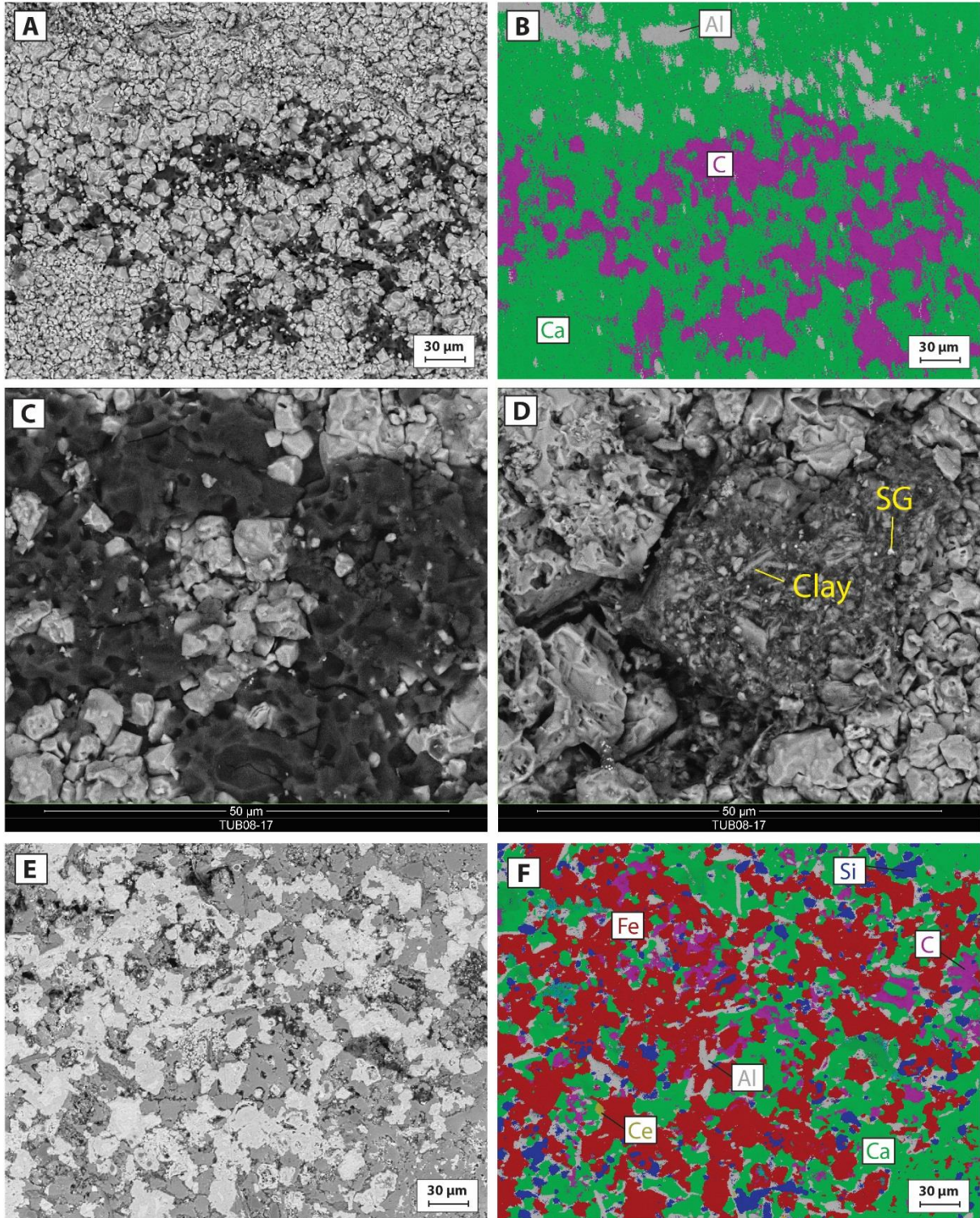


Fig. 6: SEM images and EDS elemental mapping in the organic microbial boundstone (F1c). **A-B)** Micritic to microsparitic peloids in an alveolar organic network (A) and EDS element mapping (B). On the EDS map, calcite peloids are green (Ca-rich), the alveolar organic matrix (probable EPS remnants) is pink (C-rich), while clays are grey (Al-rich). **C)** Close-up view of Fig. 6A. **D)** Organic matter-clay aggregate. Small bright sulfur rich globules (SG) are also locally observed. **E-F)** SEM picture (E) and EDS map (F) of a peloidal lamina. Calcite peloids (green) are surrounded by a mix of quartz (Si-rich; blue), clay (grey) and iron oxides (red).

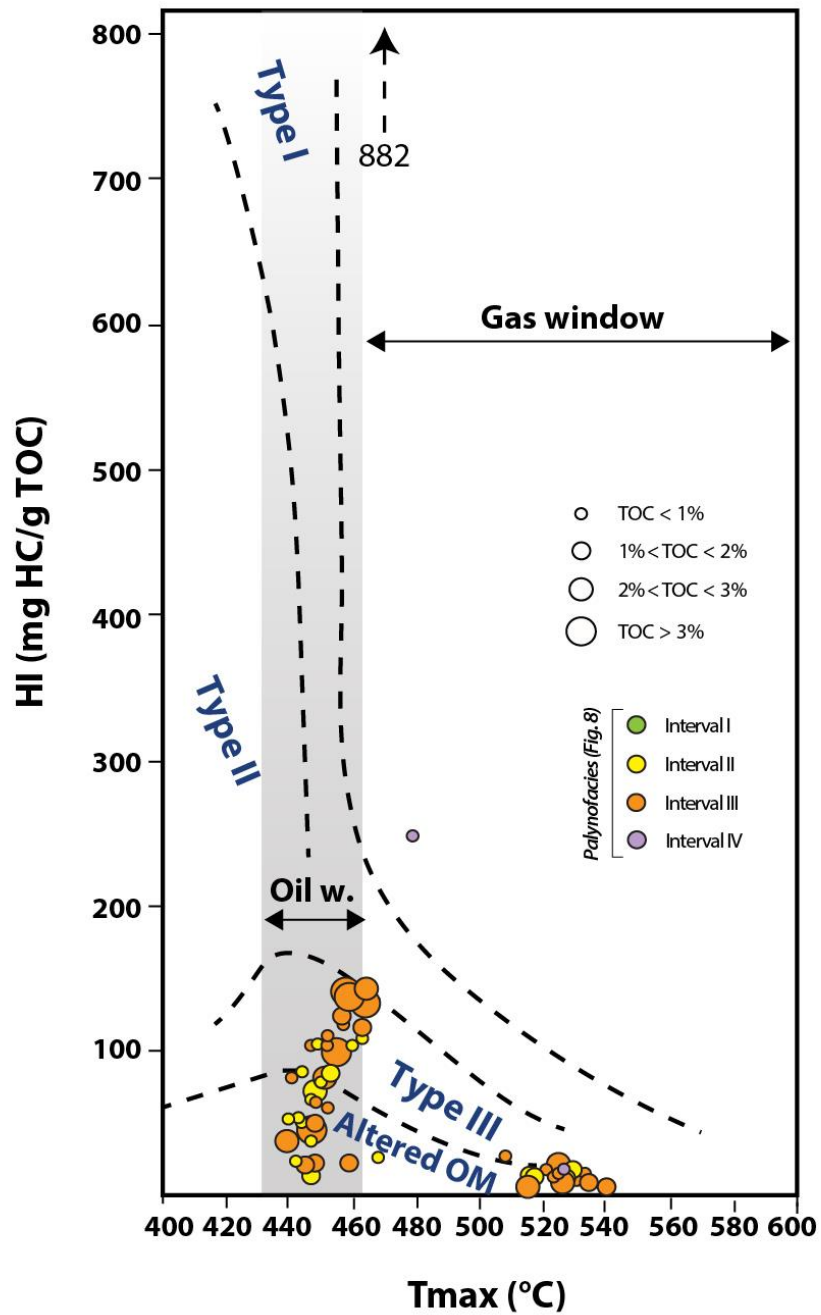


Fig. 7: Hydrogen index (HI) versus T_{max} diagram. Circle diameter is proportional to TOC, and their color is related to the palynofacies intervals defined on Figure 8.

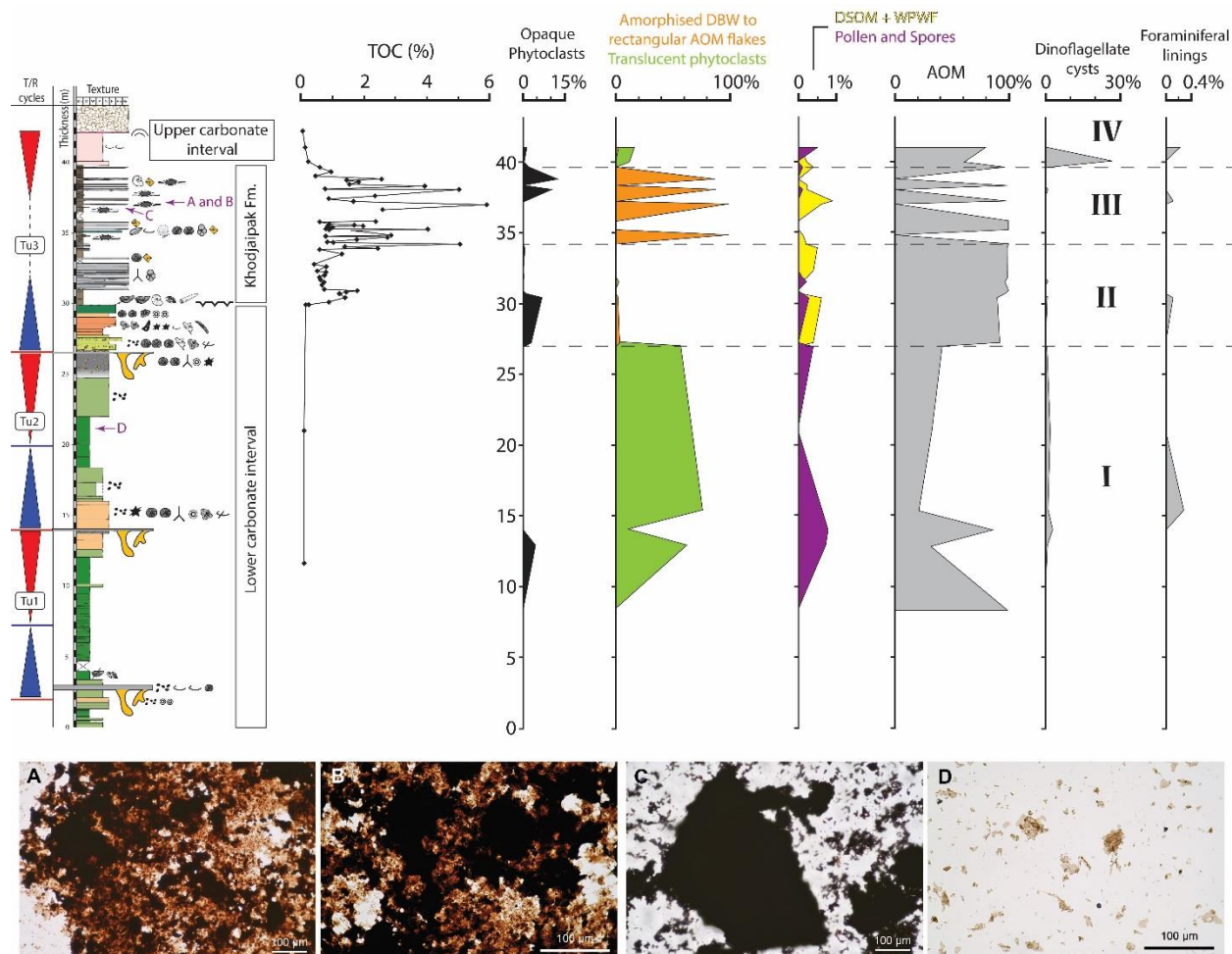


Fig. 8: Vertical evolution of palynofacies. DBW, degraded brown wood; AOM, amorphous organic matter; DSOM, dark structureless organic matter; WPF, well-preserved wood fragments. **A to D)** Palynofacies photomicrographs. **A-B)** Orange to dark amorphous organic matter (AOM), sample 09-E3, 37.2 m. **C)** Dark AOM with rectangular shape, sample 09-E2, 37 m. **D)** Translucent phytoclasts, sample 13-E4, 21 m.

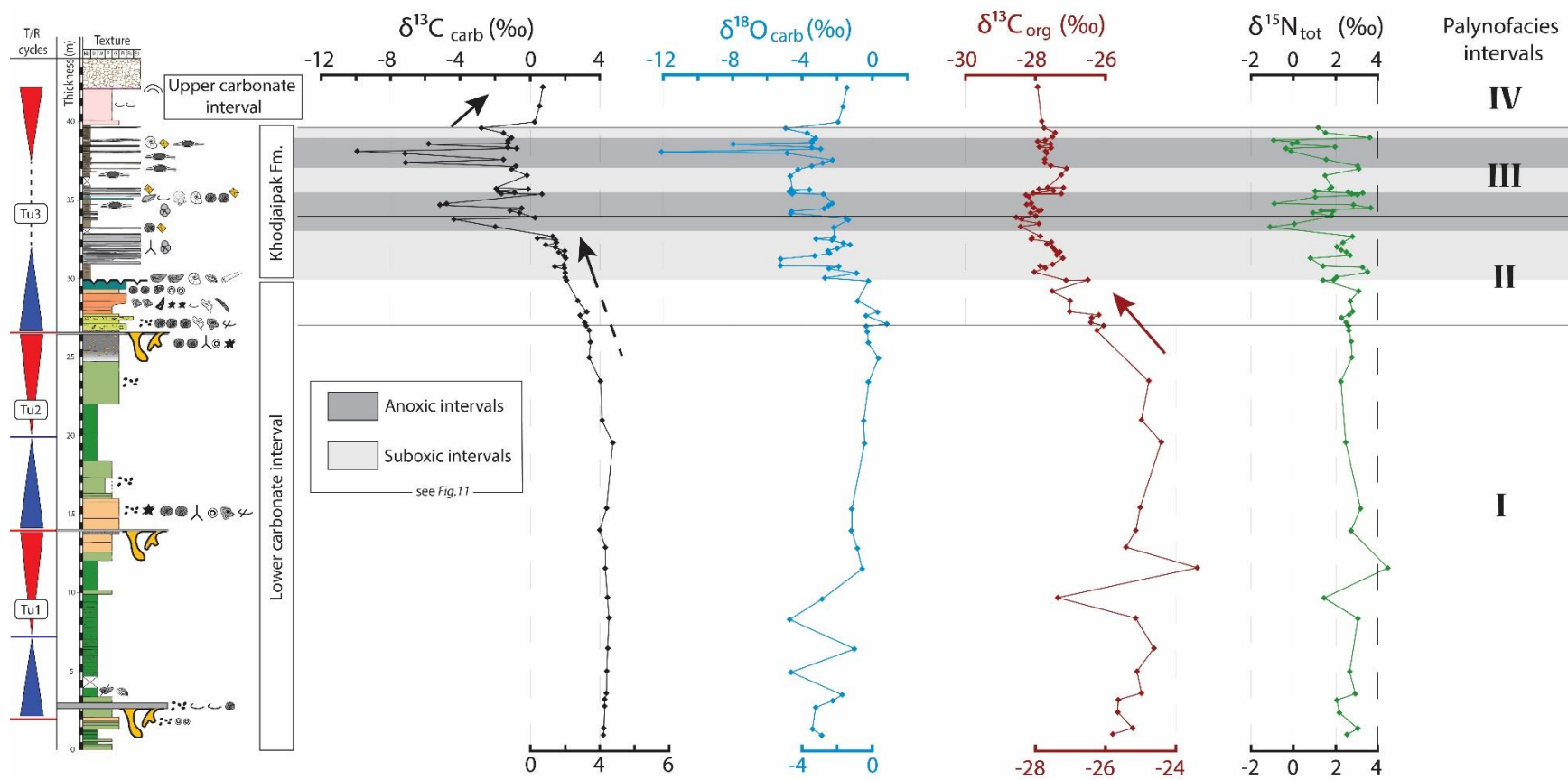


Fig. 9: Vertical evolution of organic ($\delta^{13}C_{org}$), inorganic ($\delta^{13}C_{carb}$ and $\delta^{18}O_{carb}$) and total ($\delta^{15}N_{tot}$) isotope ratio along the Tubiegatan section.

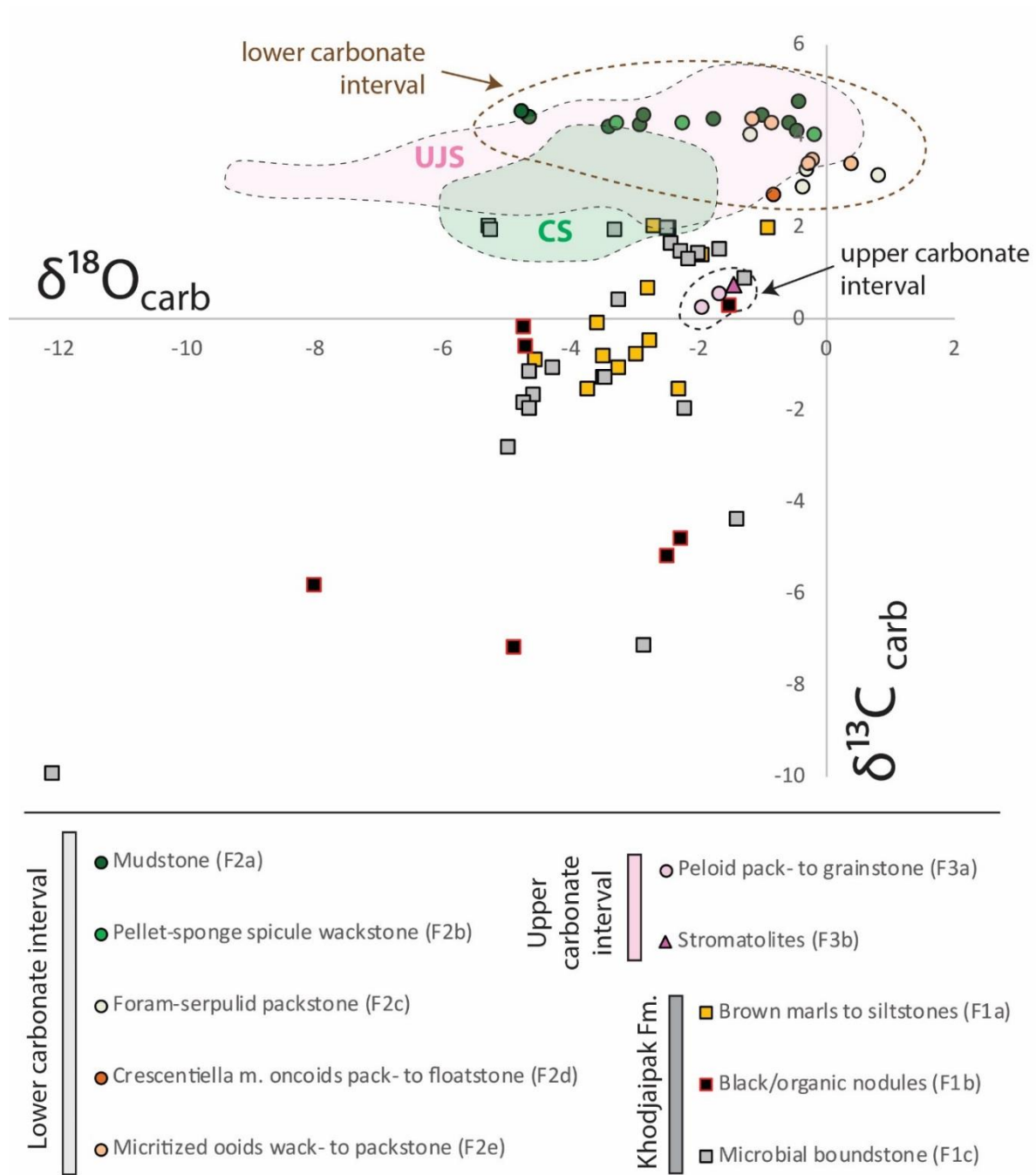


Fig. 10: $\delta^{13}\text{C}_{\text{carb}}-\delta^{18}\text{O}_{\text{carb}}$ cross-plots for the Tubiegatan section: Khodjaipak Fm., lower and upper carbonate intervals. The range of values for the south west Gissar platform carbonates (Callovian Sequence in green; Upper Jurassic Sequence in pink) are indicated.

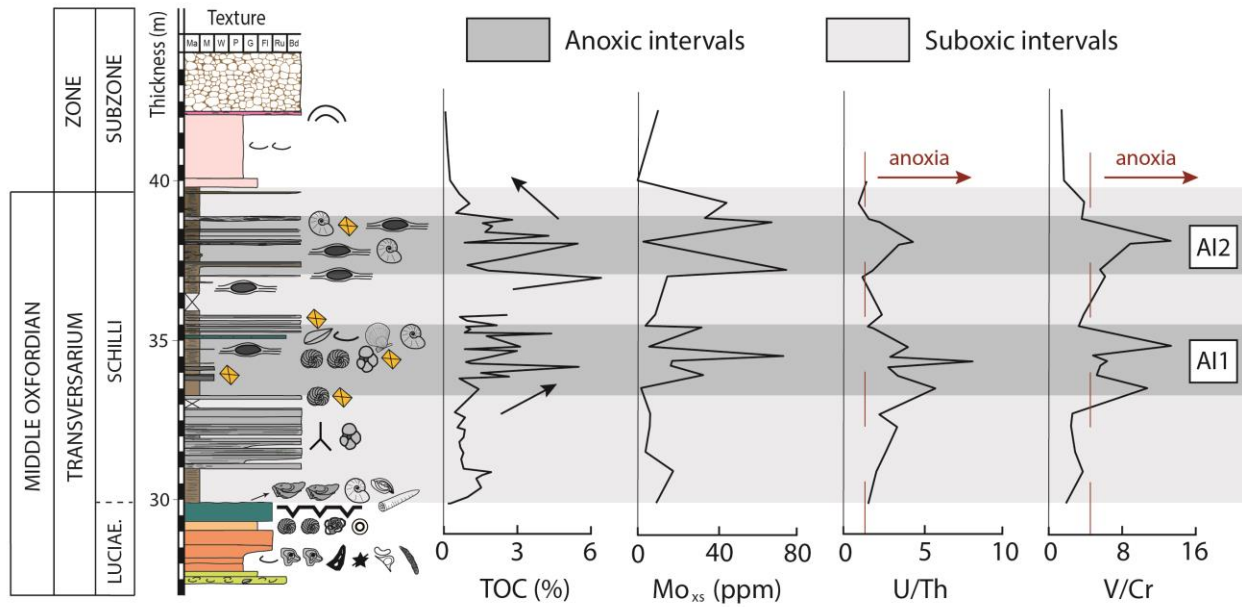
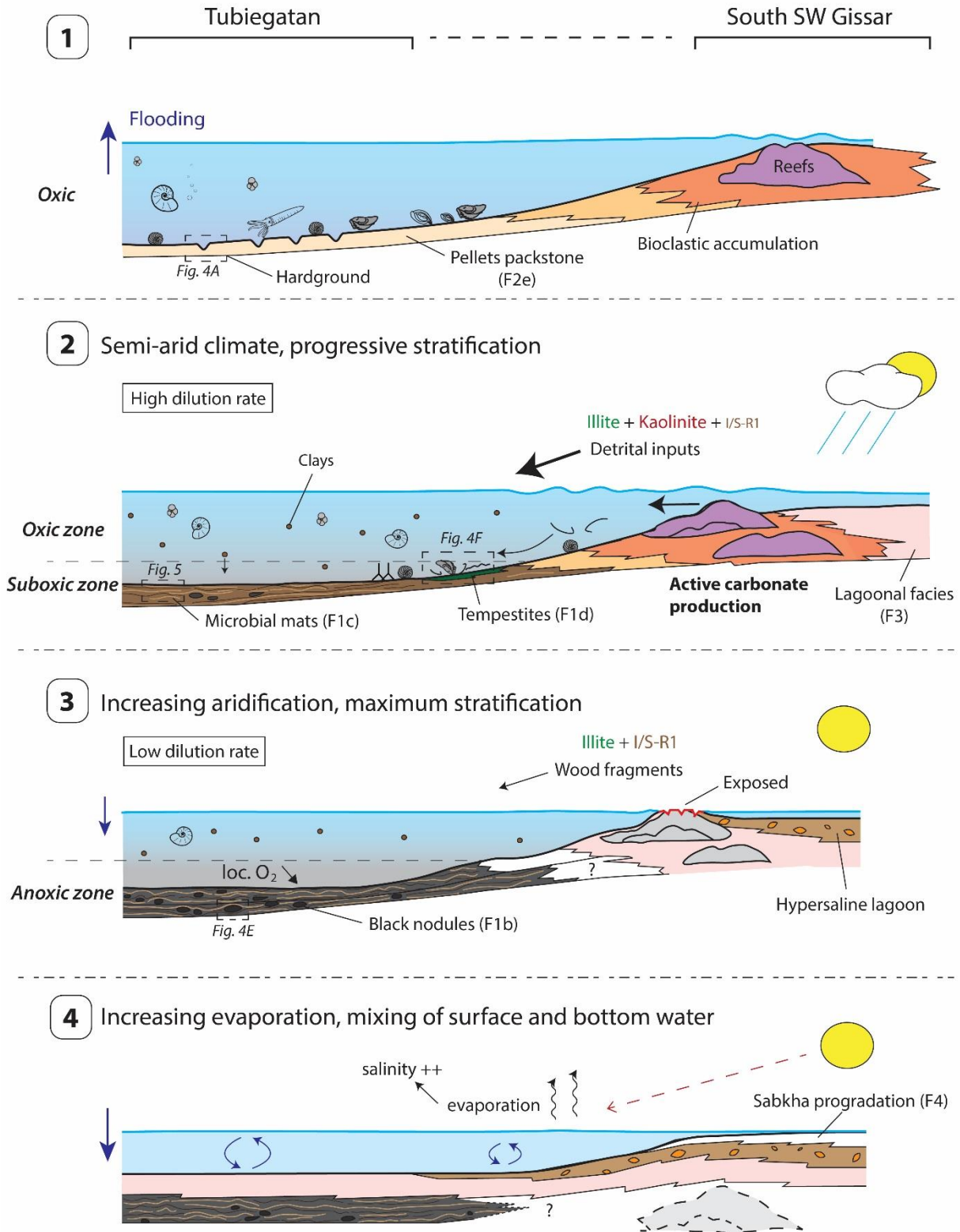


Fig. 11: Vertical evolution of TOC, Mo_{xs} and some trace metal elemental ratios: U/Th and V/Cr along the Khodjaipak Fm. Within grey intervals (AI1 and AI2), the ratios point to anoxic conditions.

A. Depositional scenario



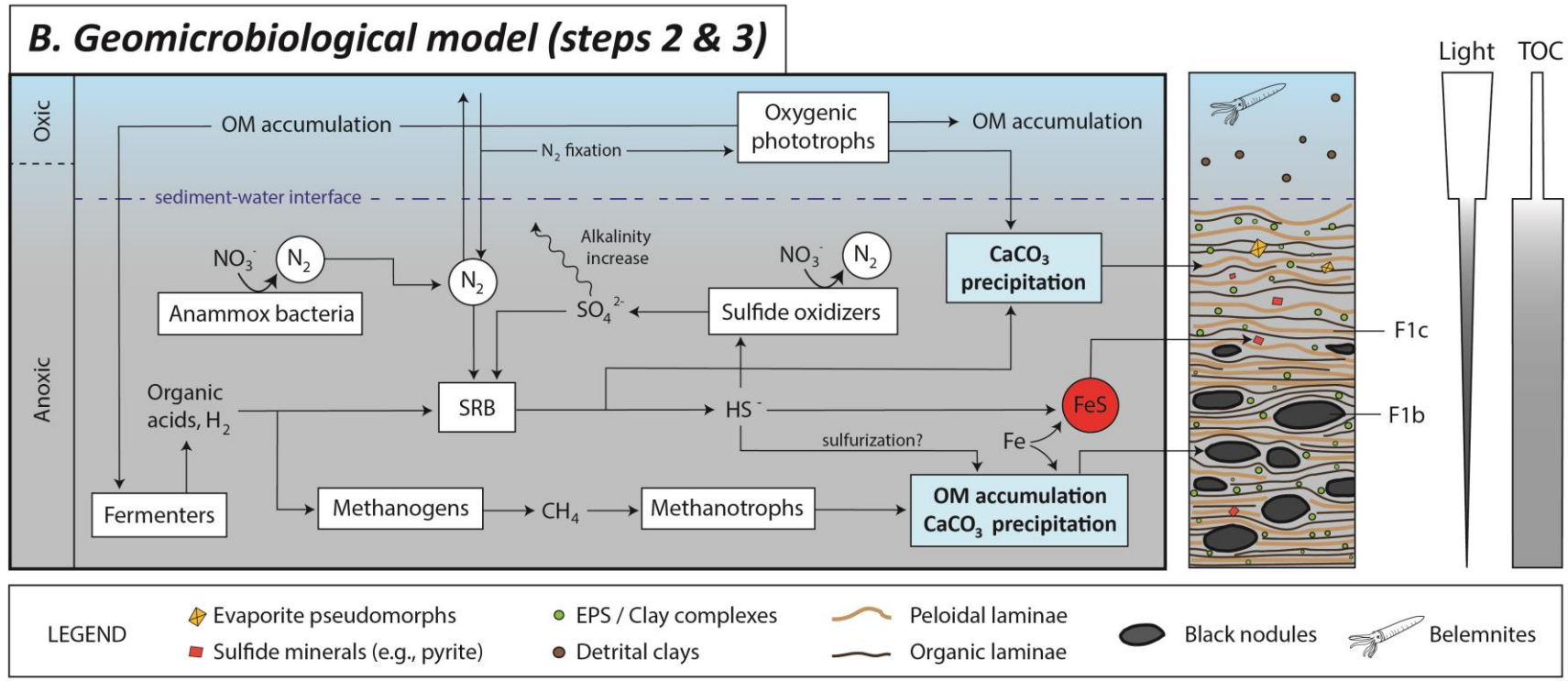
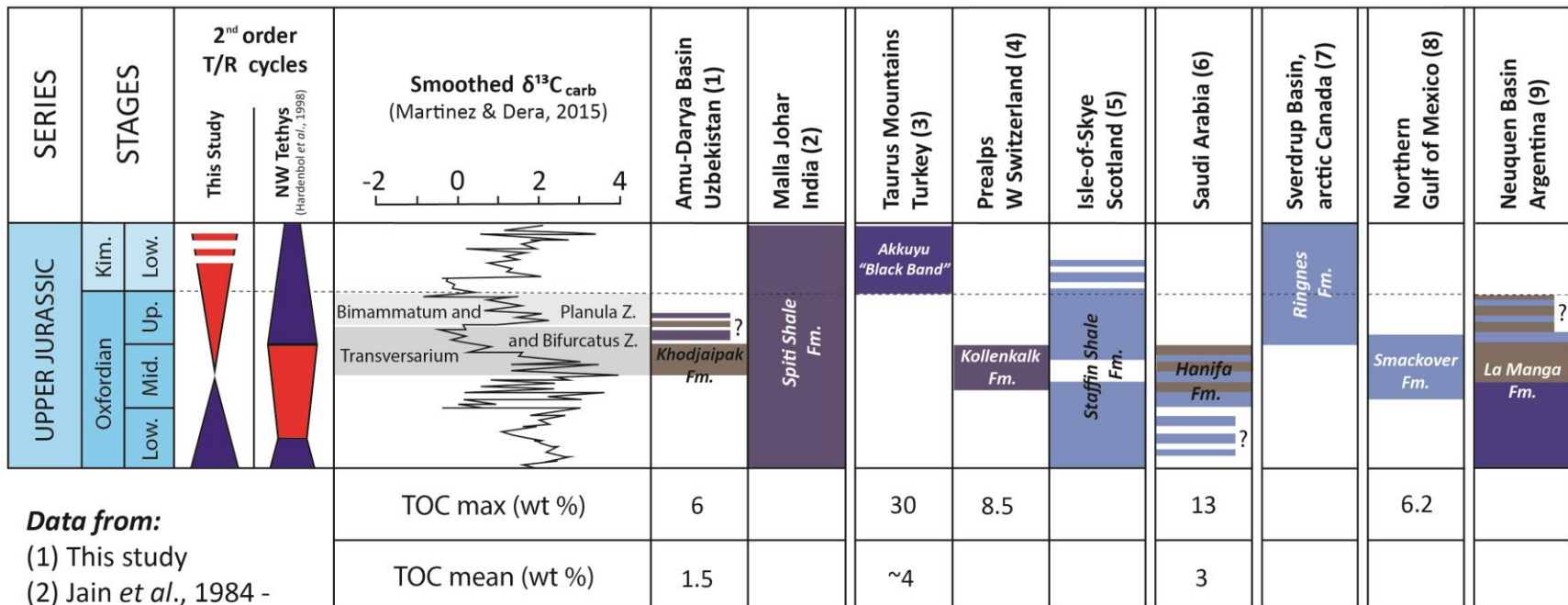


Fig. 13: (A) Depositional scenario and (B) geomicrobiological model for the Khodjaipak Fm. in the Tubiegatan area, and relationship with the SW Gissar carbonate platform.



Data from:

- (1) This study
- (2) Jain *et al.*, 1984 -
Jadoul *et al.*, 1998
- (3) Baudin *et al.*, 1999
- (4) Rais *et al.*, 2007
- (5) Pearce *et al.*, 2005
- (6) Enay *et al.*, 1987 -
Sharland *et al.*, 2001 -
Al-Husseini *et al.*, 2006
- (7) Mukhopadhyay
et al., 1997
- (8) Heydari *et al.*, 1997
Hammes *et al.*, 2011
- (9) Palma *et al.*, 2015

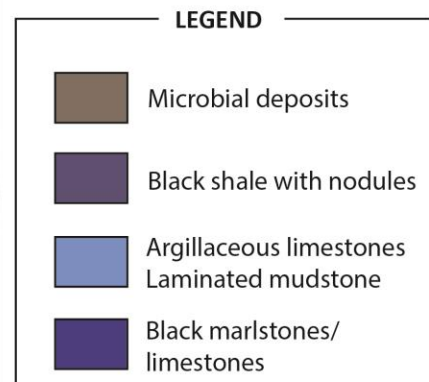
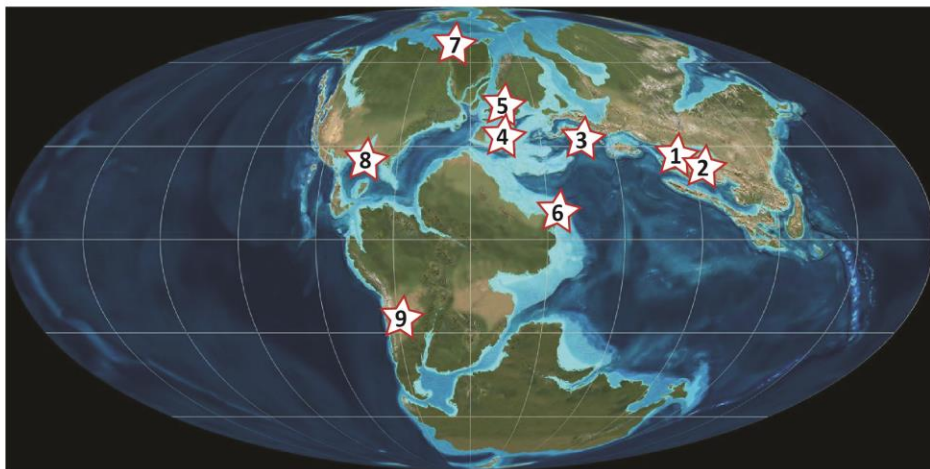


Fig. 14: Age, composition and distribution of the OM-rich sedimentary formation during the Oxfordian-Early Kimmeridgian period. The second-order NW Tethyan T/R cycles are from Hardenbol *et al.*, 1998. The smoothed $\delta^{13}\text{C}_{\text{carb}}$ curve is from Martinez and Dera, 2015.

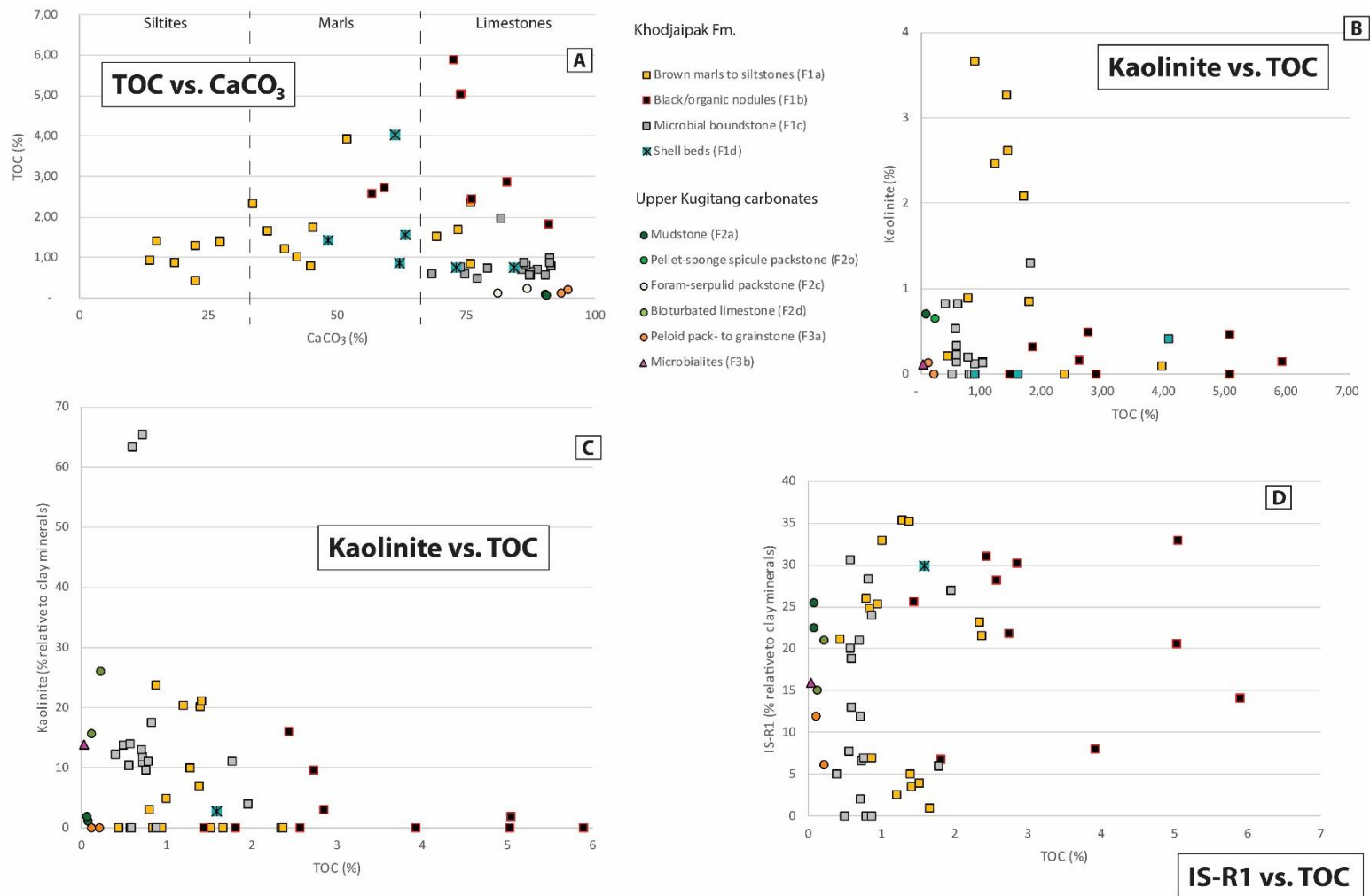


Fig. S1: **A)** Plot of CaCO₃ vs. TOC values for the Tubiegatan samples. Note that the highest values are associated to carbonate samples. **B-C)** Kaolinite vs. TOC: **(B)** percentage of kaolinite relative to bulk rock and **(C)** percentage of kaolinite relative to the clay fraction. **D)** R1-type illite-smectite mixed-layer (IS-R1) vs. TOC. The percentage of IS-R1 is relative to the clay fraction.

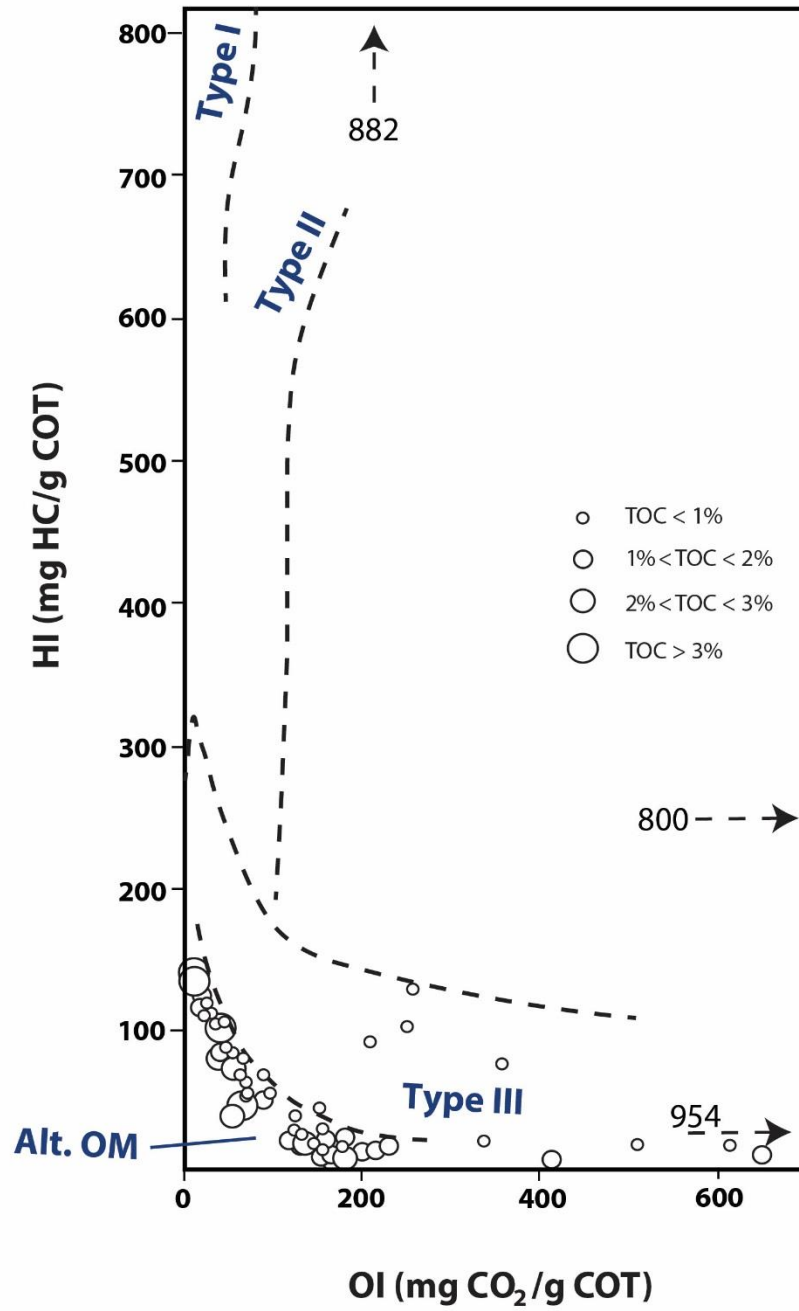


Fig. S2: Van Krevelen diagram: Hydrogen index (HI) vs. oxygen index (OI).

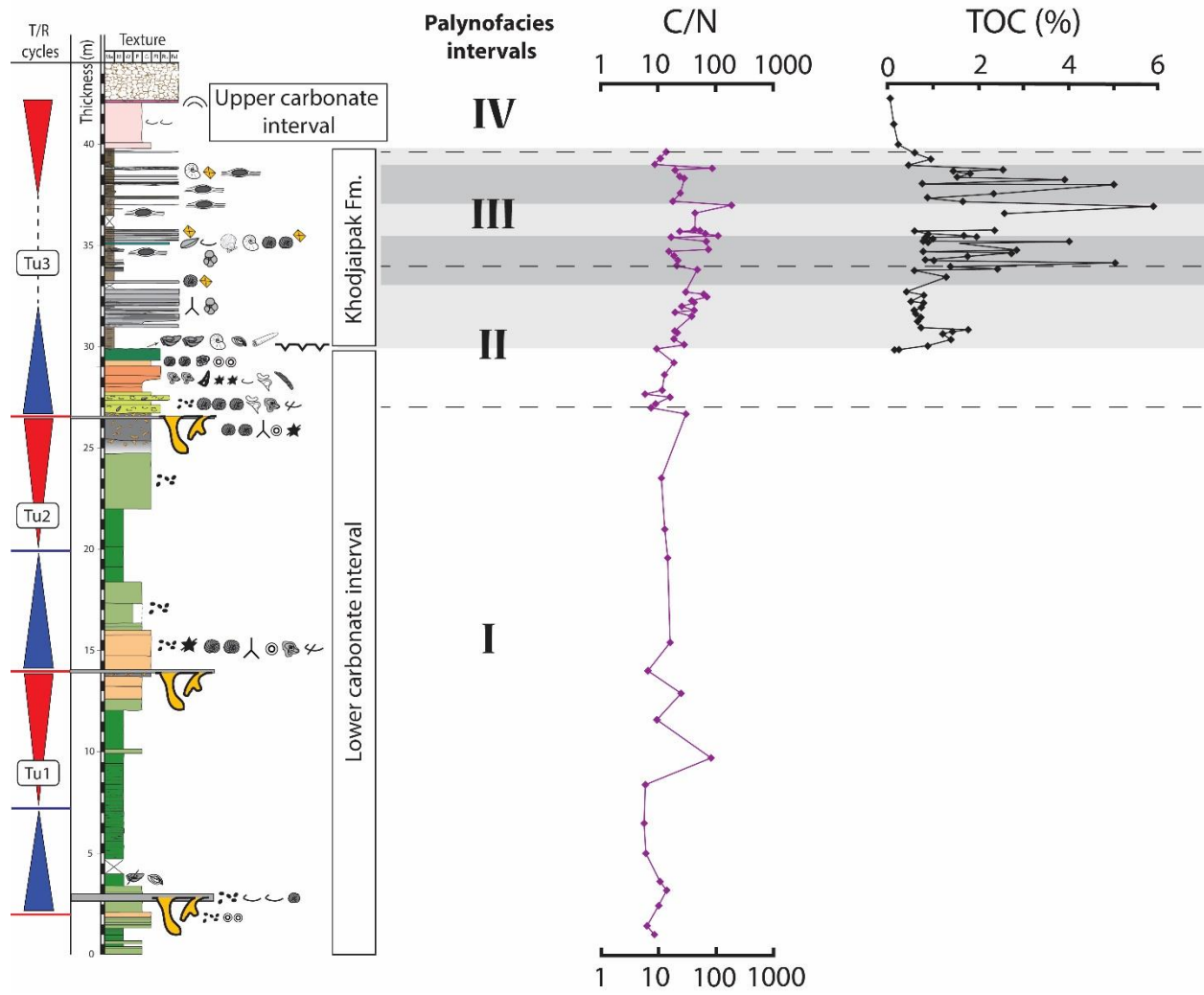


Fig. S3: Vertical evolution of the C/N ratio.